ISSN 1949-8470 (online)

World Journal of *Radiology*

World J Radiol 2023 November 28; 15(11): 304-337

Published by Baishideng Publishing Group Inc

World Journal of Radiology

Contents

Monthly Volume 15 Number 11 November 28, 2023

ORIGINAL ARTICLE

Retrospective Study

Basic Study

META-ANALYSIS

World Journal of Radiology

Monthly Volume 15 Number 11 November 28, 2023

Contents

ABOUT COVER

Peer Reviewer of *World Journal of Radiology*, Melissa Bersanelli, MD, Adjunct Professor, Chief Doctor, Medical Oncology Unit, University Hospital of Parma, Parma 43126, Italy. bersamel@libero.it

AIMS AND SCOPE

The primary aim of *World Journal of Radiology* (*WJR*, *World J Radiol*) is to provide scholars and readers from various fields of radiology with a platform to publish high-quality basic and clinical research articles and communicate their research findings online.

WJR mainly publishes articles reporting research results and findings obtained in the field of radiology and covering a wide range of topics including state of the art information on cardiopulmonary imaging, gastrointestinal imaging, genitourinary imaging, musculoskeletal imaging, neuroradiology/head and neck imaging, nuclear medicine and molecular imaging, pediatric imaging, vascular and interventional radiology, and women's imaging.

INDEXING/ABSTRACTING

The *WJR* is now abstracted and indexed in PubMed, PubMed Central, Emerging Sources Citation Index (Web of Science), Reference Citation Analysis, China National Knowledge Infrastructure, China Science and Technology Journal Database, and Superstar Journals Database. The 2023 Edition of Journal Citation Reports® cites the 2022 impact factor (IF) for *WJR* as 2.5; IF without journal self cites: 2.3; 5-year IF: 2.5; Journal Citation Indicator: 0.54.

RESPONSIBLE EDITORS FOR THIS ISSUE

NAME OF JOURNAL
World Journal of Radiology

ISSN
ISSN 1949-8470 (online)

LAUNCH DATE
January 31, 2009

FREQUENCY
Monthly

EDITORS-IN-CHIEF
Thomas J Vogl

EDITORIAL BOARD MEMBERS
https://www.wjgnet.com/1949-8470/editorialboard.htm

PUBLICATION DATE
November 28, 2023

INSTRUCTIONS TO AUTHORS
https://www.wjgnet.com/bpg/gerinfo/204

GUIDELINES FOR ETHICS DOCUMENTS
https://www.wjgnet.com/bpg/GerInfo/287

GUIDELINES FOR NON-NATIVE SPEAKERS OF ENGLISH
https://www.wjgnet.com/bpg/gerinfo/240

PUBLICATION ETHICS
https://www.wjgnet.com/bpg/GerInfo/288

PUBLICATION MISCONDUCT
https://www.wjgnet.com/bpg/gerinfo/208

ARTICLE PROCESSING CHARGE
https://www.wjgnet.com/bpg/gerinfo/242

STEPS FOR SUBMITTING MANUSCRIPTS
https://www.wjgnet.com/bpg/GerInfo/239

ONLINE SUBMISSION
https://www.f6publishing.com

World Journal of Radiology

Submit a Manuscript: https://www.f6publishing.com

World J Radiol 2023 November 28; 15(11): 304-314

DOI: 10.4329/wjr.v15.i11.304

ISSN 1949-8470 (online)

ORIGINAL ARTICLE

Retrospective Study

Radiomics analysis with three-dimensional and two-dimensional segmentation to predict survival outcomes in pancreatic cancer

Mohammed Saleh, Mayur Virarkar, Hagar S Mahmoud, Vincenzo K Wong, Carlos Ignacio Gonzalez Baerga, Miti Parikh, Sherif B Elsherif, Priya R Bhosale

Specialty type: Radiology, nuclear medicine and medical imaging

Provenance and peer review: Invited article; Externally peer reviewed.

Peer-review model: Single blind

Peer-review report's scientific quality classification

Grade A (Excellent): 0
Grade B (Very good): B
Grade C (Good): C
Grade D (Fair): 0
Grade E (Poor): 0

P-Reviewer: Lin W, China

Received: August 28, 2023
Peer-review started: August 28, 2023
First decision: September 19, 2023
Revised: September 20, 2023
Accepted: October 23, 2023
Article in press: October 23, 2023
Published online: November 28, 2023

Mohammed Saleh, Hagar S Mahmoud, Vincenzo K Wong, Priya R Bhosale, Department of Diagnostic Radiology, The University of Texas MD Anderson Cancer Center, Houston, TX 77030, United States

Mayur Virarkar, Carlos Ignacio Gonzalez Baerga, Sherif B Elsherif, Department of Diagnostic Radiology, The University of Florida College of Medicine, Jacksonville, FL 32209, United States

Miti Parikh, Keck School of Medicine, University of South California, Los Angeles, CA 90033, United States

Corresponding author: Carlos Ignacio Gonzalez Baerga, MD, Research Assistant, Department of Diagnostic Radiology, The University of Florida College of Medicine, 655 8th Street West, Jacksonville, FL 32209, United States. carlos.gonzalezbaerga@jax.ufl.edu

Abstract

BACKGROUND

Radiomics can assess prognostic factors in several types of tumors, but considering its prognostic ability in pancreatic cancer has been lacking.

AIM

To evaluate the performance of two different radiomics software in assessing survival outcomes in pancreatic cancer patients.

METHODS

We retrospectively reviewed pretreatment contrast-enhanced dual-energy computed tomography images from 48 patients with biopsy-confirmed pancreatic ductal adenocarcinoma who later underwent neoadjuvant chemoradiation and surgery. Tumors were segmented using TexRad software for 2-dimensional (2D) analysis and MIM software for 3D analysis, followed by radiomic feature extraction. Cox proportional hazard modeling correlated texture features with overall survival (OS) and progression-free survival (PFS). Cox regression was used to detect differences in OS related to pretreatment tumor size and residual tumor following treatment. The Wilcoxon test was used to show the relationship between tumor volume and the percent of residual tumor. Kaplan-Meier analysis was used to compare survival in patients with different tumor densities in Hounsfield units for both 2D and 3D analysis.

RESULTS
3D analysis showed that higher mean tumor density [hazard ratio (HR) = 0.971, P = 0.041)] and higher median tumor density (HR = 0.970, P = 0.037) correlated with better OS. 2D analysis showed that higher mean tumor density (HR = 0.963, P = 0.014) and higher mean positive pixels (HR = 0.962, P = 0.014) correlated with better OS; higher skewness (HR = 3.067, P = 0.008) and higher kurtosis (HR = 1.176, P = 0.029) correlated with worse OS. Higher entropy correlated with better PFS (HR = 0.056, P = 0.036). Models determined that patients with increased tumor size greater than 1.35 cm were likely to have a higher percentage of residual tumors of over 10%.

CONCLUSION
Several radiomics features can be used as prognostic tools for pancreatic cancer. However, results vary between 2D and 3D analyses. Mean tumor density was the only variable that could reliably predict OS, irrespective of the analysis used.

Key Words: Radiomics; Pancreas; Cancer; Segmentation

Core Tip: The use of radiomics to assess pancreatic cancer has been limited. This retrospective study evaluated the performance of 2-dimensional (2D) and 3D radiomic software in determining survival outcomes of pancreatic cancer patients. The mean tumor density was the only variable to reliably predict overall survival (OS) irrespective of the type of analysis. Mean tumor density may be able to differentiate survival and potentially may be help in treatment planning irrespective of the texture analysis software used. Higher skewness [hazard ratio (HR) = 3.067, P = 0.008] and higher kurtosis (HR = 1.176, P = 0.029) correlated with worse OS based on 2D analysis.

Citation: Saleh M, Virarkar M, Mahmoud HS, Wong VK, Gonzalez Baerga CI, Parikh M, Elsherif SB, Bhosale PR. Radiomics analysis with three-dimensional and two-dimensional segmentation to predict survival outcomes in pancreatic cancer. *World J Radiol* 2023; 15(11): 304-314
URL: https://www.wjgnet.com/1949-8470/full/v15/i11/304.htm
DOI: https://dx.doi.org/10.4329/wjr.v15.i11.304

INTRODUCTION

Pancreatic cancer is an aggressive malignancy causing 7%-8% of cancer-related deaths in the United States[1]. The 5-year overall survival (OS) rate is currently less than 5% despite aggressive multimodality treatment approaches, which mainly include neoadjuvant chemoradiation followed by surgery[2,3]. Up to 60% of patients experience recurrence following definitive therapy[3-5]. Pretreatment stratification of patients based on risk of recurrence and mortality may help determine the aggressiveness of the treatment plan and guide optimal management.

Several risk factors may affect pancreatic cancer prognosis and OS, such as vascular invasion, lymph node metastasis, tumor stage, and tumor differentiation[6]. Although some prognostic factors may be evaluated by conventional imaging, several others require invasive histologic assessment, which is expensive, carries the risk of complications such as infections or bleeding, and may not provide a complete evaluation of the tumor owing to sampling variability.

There is increasing interest in radiomics because it converts qualitative and subjective imaging data into quantitative and objective data through complex algorithms to provide information that a radiologist cannot extract with the naked eye. Several studies have demonstrated that radiomics can noninvasively assess tumor grade, lymph node metastasis, and other prognostic factors for multiple types of tumors[7-9]. However, only a few studies have evaluated the use of radiomics for assessing prognosis for pancreatic tumors[10-13]. Additionally, texture analysis values extracted *via* artificial intelligence programs are software-dependent and may vary among software programs due to differing algorithms and processing. For example, MIM performs a 3-dimensional (3D) volumetric analysis, whereas TexRad performs a cross-sectional 2D analysis of only a single slice.

Given this discrepancy, the primary objective of the current study was to determine whether pancreatic tumor texture features can reliably be used as prognostic indicators to provide reproducible results independent of the artificial intelligence software or type of analysis used.

MATERIALS AND METHODS

Patients

This retrospective single-center study was reviewed and approved by the Institutional Review Board in compliance with HIPAA guidelines. Institutional records between January 2012 and November 2020 were accessed. Our inclusion criteria

included patients undergoing a baseline (pretreatment) contrast-enhanced dual-energy computed tomography (CT) study of the primary pancreatic tumor before chemoradiation and subsequent surgery. Patients who did not have: (1) Baseline pretreatment CT study data; (2) Histologic confirmation of a primary tumor of the pancreas; and/or (3) Visible tumors on the CT study were excluded from the analysis. Forty-eight patients met the inclusion criteria. An undergraduate research student searched the patients' medical records for date of birth, date of first CT study, date of diagnosis, date of last follow-up, date of surgery, histological tumor size, tumor histologic characteristics, and histologic differentiation, presence of adenopathy, both before and after treatment, type of neoadjuvant therapy received, recurrence state, date of recurrence, vital status, and date of death, if applicable. Tumor responses were based on a comparative evaluation of pre- and post-treatment scans and were evaluated by the Response Evaluation Criteria in Solid Tumors criteria.

CT protocol and image acquisition

All patients underwent the pretreatment abdominal contrast-enhanced dual-energy CT study *via* a 64-detector row Discovery CT750 HD CT scanner (Gemstone Spectral Imaging, GE Healthcare, Milwaukee, WI) with a multiphasic pancreatic protocol with rapid switching. Images were acquired intravenously after injecting 125-150 mL of Omnipaque 350 (Mallinckrodt, St Louis, MO) at a rate of 4-5 mL/s. Bolus tracking was used. When a 100-Hounsfield unit (HU) increase was detected at the origin of the celiac axis, images were obtained with a diagnostic scan delay of 20 s, from the level of the hemidiaphragm to the iliac crest, using a rapid switching dual-energy technique (80 kVp and 140 kVp). The scan duration was 5 s for the abdomen. The late arterial/pancreatic parenchymal phase was obtained approximately 40-45 s after the start of contrast injection, and an additional 20-s delay scan using a 120-kVp conventional non-dual-energy imaging technique, resulting in a portal venous phase, was obtained approximately 65-70 s after the start of contrast injection. Images in the pancreatic parenchymal and portal venous phases were reconstructed at 2.5-mm slice thickness. The scan parameters were as follows: Tube current 125-600 ms, tube voltage 120 kVp, pitch 0.98:1, slice thickness 0.6-5 mm, revolution time 0.8 s, table feed speed 39.375 mm/rotation, and field of view 440 mm.

Radiomics workflow

Our study included two separate segmentation programs: MIM software version 6.9.4 (MIM Software Inc) and TexRad Research version 3.9 (Cambridge Computed Imaging LTD). Both radiomics workflows started with tumor segmentation on the treatment-naïve imaging studies, followed by feature extraction. The tumors were segmented by a research fellow in the abdominal radiology department under the supervision of an oncologic radiologist with ten years of experience.

3D segmentation: The portal venous phase was used for segmentation. The tumors were contoured on MIM software using the 3D brush on the axial, coronal, and sagittal planes (Figure 1) by an abdominal radiologist with ten years of clinical experience. A research fellow assisted in extracting the texture features on MIM and saved them on an encrypted server. Seventeen texture features [integral total value (HU × Ml), kurtosis, maximum HU, mean HU, maximum mean HU ratio, median HU, median minimum HU ratio, minimum HU, minimum mean HU ratio, skewness, sphere value (cm), standard deviation, standard deviation mean HU ratio, total HU, volume, voxel count, and entropy], all belonging to first-order statistics, were extracted *via* an algorithm developed by MIM Software Inc for the texture analysis of CT scans (Table 1).

2D segmentation: The images evaluated in 2D segmentation were also derived from the portal venous phase uploaded to the commercially available TexRad research software. 2D segmentation was performed using the polygon region of interest tool. The slice with the greatest tumor diameter was used, and textural radiomic features were extracted automatically from the images within the region of interest. A total of 6 texture features (entropy, kurtosis, mean HU, mean positive pixels, skewness, and standard deviation) were extracted. Because TexRad software applies spatial scale filters and MIM's algorithm does not, only values without using a spatial scale filter were considered to compare the two software programs.

Statistical analyses

For 2D and 3D analysis, the correlation between tumor size and percentage of residual tumor based on histological evaluation was assessed using simple linear regression. The Wilcoxon test was used to show the relationship between tumor volume and the percent of residual tumor. The Youden index was used to determine the optimal cutoff for predicting residual tumors based on tumor size. Also, a receiver operating characteristic curve was generated to predict the performance of tumor size in estimating residual tumors.

Simple logistic regression was used to correlate the texture features with post-treatment adenopathy. A Cox proportional hazards model was used to fit univariate models identifying associations between texture features and OS and progression-free survival (PFS). Cox regression was used to detect any significant association between OS and the percentage of residual tumor following treatment or tumor size.

For 2D and 3D analysis, recursive partitioning analysis was carried out using the R package "rpart" to identify a cutoff that can predict OS by mean HU value. All tests were two-sided, and $P < 0.05$ was considered statistically significant. Statistical analysis was done using SAS version 9.4 (SAS Institute, Cary, NC). The Kaplan-Meier analysis was used to compare survival in patients with different tumor densities in HU for both 2D and 3D analysis.

Table 1 Radiomic features extracted from segmentation programs

MIM Software Inc (3D segmentation)	Cambridge Computed Imaging LTD (2D segmentation)
Integral total value	Entropy
Kurtosis	Kurtosis
Maximum HU	Mean HU
Mean HU	Mean positive pixels
Maximum mean HU ratio	Skewness
Median HU	Standard deviation
Median minimum HU ratio	
Minimum HU	
Minimum mean HU ratio	
Skewness	
Sphere value	
Standard deviation	
Standard deviation mean HU ratio	
Total HU	
Volume	
Voxel count	
Entropy	

HU: Hounsfield units; 2D: Two-dimensional; 3D: Three-dimensional.

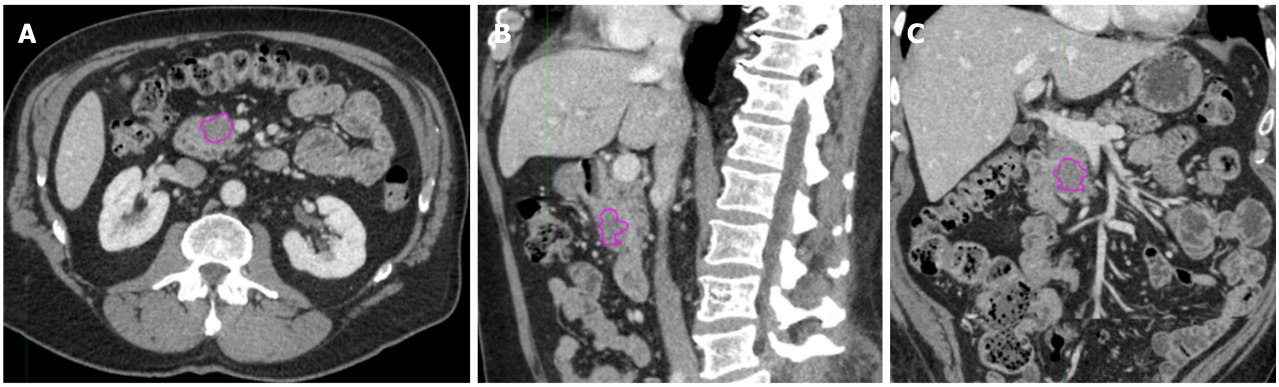

DOI: 10.4329/wjr.v15.i11.304

Figure 1 Example of contouring using the 3-dimensional brush on MIM software in the different planes. A: Axial; B: Sagittal; C: Coronal.

RESULTS

The patients' mean ± SD age was 61.2 ± 12.8 years, with a median age of 61.9. Patient ages ranged from 18.6 years to 88.9 years. Linear regression showed that histologic tumor size was correlated with residual tumor [correlation coefficient = 0.51, 95% confidence interval (CI): 0.26-0.70, Figure 2]. Using a cutoff of 1.35 cm, based on histologic tumor size, our models showed that patients with a tumor size greater than 1.35 cm are at risk of having more than 10% residual tumor (sensitivity = 0.64, specificity = 0.94, accuracy = 0.85, P = 0.015; Figures 3 and 4).

3D analysis

Linear regression showed that histologic tumor size was correlated with residual tumor (correlation coefficient = 0.51, 95%CI: 0.26-0.70, Figure 2). Using a cutoff of 1.35 cm, based on histologic tumor size, our models showed that patients with a tumor size greater than 1.35 cm are at risk of having more than 10% residual tumor (sensitivity = 0.64, specificity = 0.94, accuracy = 0.85, P = 0.015; Figures 3 and 4).

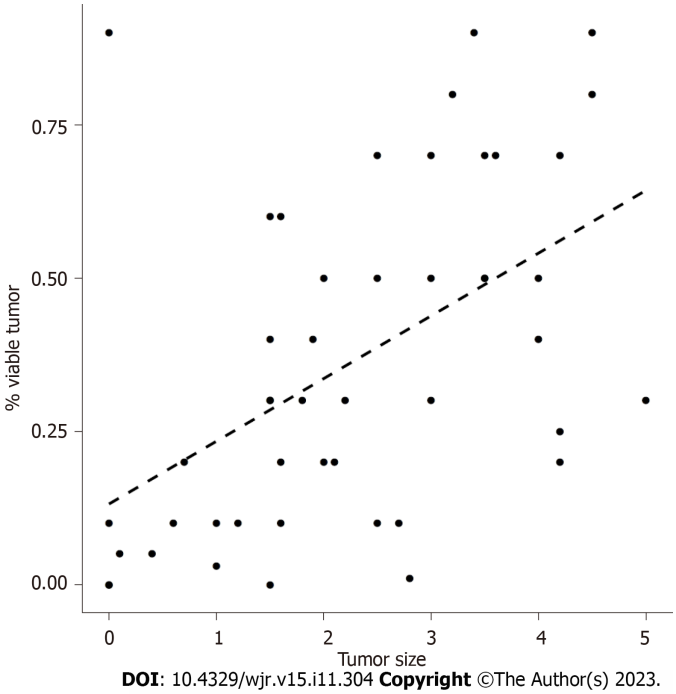

DOI: 10.4329/wjr.v15.i11.304 **Copyright** ©The Author(s) 2023.

Figure 2 Linear regression showing that residual tumor was significantly linearly correlated with tumor size (*P* = 0.0002). Using tumor size as the predictor (x-axis), the slope is 0.1023, meaning that for every single unit increase in tumor size, there is a 10.23% increase in the percentage of residual tumors.

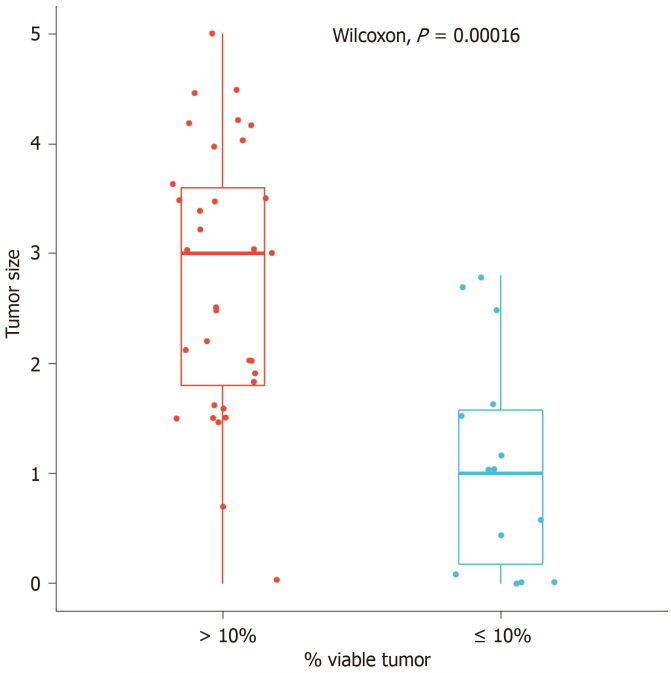

DOI: 10.4329/wjr.v15.i11.304 **Copyright** ©The Author(s) 2023.

Figure 3 Box plot showing the relationship between tumor size and residual tumor in our cohort.

Linear regression analysis showed that mean HU [correlation coefficient = -0.0040, standard error (SE) = 0.0018, *P* = 0.0326], median HU (correlation coefficient = -0.0039, SE = 0.0019, *P* = 0.0373), and minimum mean HU ratio (correlation coefficient = -0.1038, SE = 0.0499, *P* = 0.0406) were inversely correlated with the percentage of residual tumor following treatment.

The univariate Cox proportional hazards model showed that mean HU and median HU were significantly correlated with OS [mean HU: hazard ratio (HR) = 0.971, 95%CI: 0.945-0.999, *P* = 0.041; median HU: HR = 0.970, 95%CI: 0.942-0.998, *P* = 0.037]. A cutoff value of mean HU ≥ 61.185 significantly predicted better OS (*P* = 0.0039; Figure 5A). None of the texture features significantly correlated with post-treatment adenopathy or PFS risk.

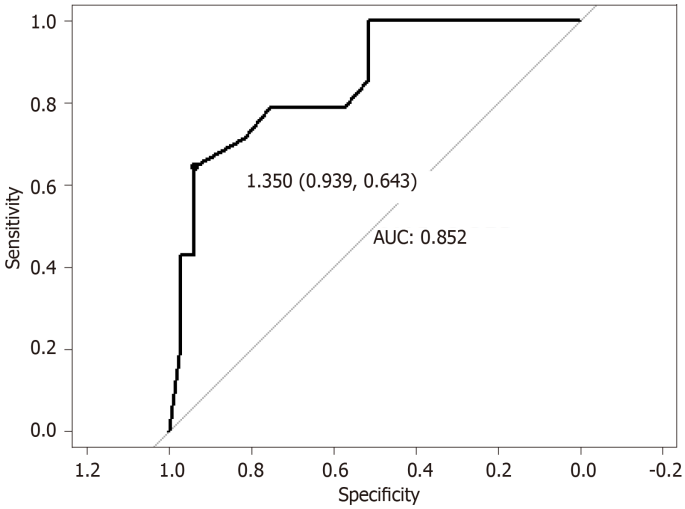

DOI: 10.4329/wjr.v15.i11.304 **Copyright** ©The Author(s) 2023.

Figure 4 Receiver operating characteristic curve showing that 1.35-cm tumor size is the optimal cutoff point for predicting ≤ 10% residual tumor, determined by the Youden index. This model predicts ≤ 10% residual tumor with an area under the curve of 0.852, sensitivity of 0.643, and specificity of 0.939. AUC: Area under the curve.

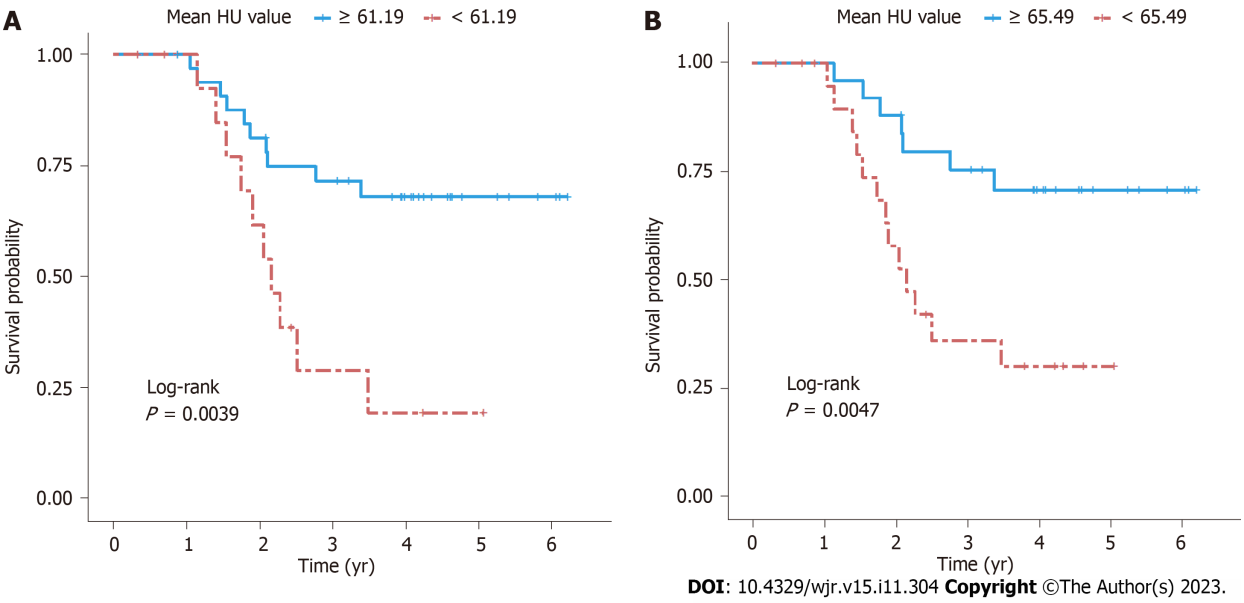

DOI: 10.4329/wjr.v15.i11.304 **Copyright** ©The Author(s) 2023.

Figure 5 Kaplan-Meier curves. A: Kaplan-Meier curves comparing patients with mean Hounsfield units (HU) value greater or less than 61.185, based on 3-dimensional analysis. Log-rank *P* = 0.0039 indicates that patients with mean HU ≥ 61.185 had significantly better overall survival than those with mean HU < 61.185; B: Kaplan-Meier curves comparing patients with mean HU value greater or less than 65.485, based on 2-dimensional analysis. Log-rank *P* = 0.0047 indicates that patients with mean HU ≥ 65.485 had significantly better overall survival than those with mean HU < 65.485. HU: Hounsfield units.

2D analysis

Without a spatial scale filter, high tumor entropy (correlation coefficient = -0.641, SE = 0.301, *P* = 0.039), increased mean HU (correlation coefficient = -0.004, SE = 0.002, *P* = 0.032), and high mean positive pixels (correlation coefficient = -0.005, SE = 0.002, *P* = 0.032) correlated with less than 10% residual tumor following treatment. Entropy is also positively associated with PFS (HR = 0.056, 95%CI: 0.004-0.831, *P* = 0.036).

For 2D values, a cutoff of 65.485 for mean HU was appropriate for differentiating mortality risk; patients with equal or higher values than the threshold had significantly better OS (*P* = 0.0047; Figure 5B). High mean positive pixels were associated with better OS (*P* = 0.014), whereas high kurtosis (*P* = 0.029) and skewness (*P* = 0.007) were associated with worse OS (Table 2). No significant correlations existed between texture features at 0 spatial scale filter and post-treatment adenopathy.

Table 2 Univariate Cox proportional hazards model for overall survival (hazard ratio < 1 indicates better prognosis)

SSF	Variable	Hazard ratio	95% CI	*P* value
0	Kurtosis	1.176	1.017-1.361	0.029
0	Mean HU	0.963	0.935-0.993	0.014
0	MPP	0.962	0.933-0.992	0.014
0	Skewness	3.067	1.345-6.993	0.008
2	Entropy	0.042	0.003-0.636	0.022
2	Mean HU	0.975	0.961-0.989	0.001
3	Mean HU	0.980	0.968-0.991	< 0.001
4	Kurtosis	1.071	1.000-1.146	0.048
4	Mean HU	0.985	0.974-0.995	0.003
4	MPP	1.012	1.000-1.023	0.046
4	SD	1.006	1.001-1.011	0.016
5	MPP	1.009	1.002-1.017	0.012
5	SD	1.006	1.001-1.011	0.010
6	MPP	1.007	1.002-1.013	0.008
6	SD	1.006	1.001-1.011	0.011

Without a spatial scale filter (SSF), patients with high kurtosis and skewness had worse overall survival. Patients with elevated mean Hounsfield units and mean positive pixels had better overall survival. Several other significant findings were found when an SSF was applied (2 through 6). HU: Hounsfield units; SSF: Spatial scale filter; MPP: Mean positive pixels; 95%CI: 95% confidence interval.

DISCUSSION

Our study suggests that baseline CT-based texture features are noninvasive prognostic indicators that can help predict residual tumors, response to therapy, and prognosis in patients with pancreatic cancer. We also found that some of these textural features are reproducible irrespective of the software or analysis used. 3D and 2D analyses showed that higher tumor density correlated with better OS and lower residual tumors. However, unlike 3D analysis, the 2D analysis also showed that higher skewness and higher kurtosis were correlated with worse OS and higher entropy was correlated with better PFS.

Our study showed that tumor density was a predictor of OS, irrespective of the texture analysis software used. The findings of Cassinotto *et al*[14] corroborate our findings. In that study, hypoattenuating pancreatic adenocarcinomas on preoperative scans were associated with worse disease-free survival. In addition, hypoattenuating tumors were associated with an increased risk of lymph node metastasis and high tumor grade, which explained the poor survival outcomes compared with patients with hyperattenuating tumors. Fukukura *et al*[15] also demonstrated that hypoattenuating pancreatic tumors on pretreatment scans may independently predict worse OS in patients undergoing surgery or receiving adjuvant treatments. Another study by Zhu *et al*[16] showed that hypoattenuating pancreatic tumors treated with surgical resection were associated with poorer disease-free survival compared with hyperattenuating pancreatic tumors. Hypoattenuating tumors have been shown to have a greater degree of necrosis, an indicator of tumor hypoxia, and, therefore, accelerated malignant potential. This radiologic-pathologic association helps explain the association of hypoattenuation with poor prognosis[17,18].

Higher tumor density (mean HU) and smaller tumor size correlated with a lower percentage of residual tumors following treatment. Our findings suggest that smaller and/or hyperattenuating tumors on the portal venous phase of contrast-enhanced CT will likely respond to chemotherapy because they showed a lower percentage of residual tumors following treatment. To our knowledge, no previous studies have evaluated this correlation. Several studies have shown that patients with pancreatic cancer showing greater than 10% residual tumor following treatment have a worse prognosis[19,20]. Okubo *et al*[21] showed that patients with residual tumors greater than 220 mm^2 had a higher risk of lymphatic, perineural, and vascular invasion. This variable was an independent predictor of a worse recurrence-free survival. In our study, hyperattenuating tumors correlated with lower residual tumors after therapy, which likely explains the correlation between higher tumor density and better survival outcomes. Therefore, using tumor density on baseline scans as a prognostic predictor could help clinicians plan management, with the higher-risk group potentially receiving more aggressive therapies or undergoing more aggressive monitoring.

2D analysis showed that skewness and kurtosis were inversely correlated with OS. Attiyeh *et al*[22] developed two separate models with 255 radiomics features that measure pixel spatial variation, including kurtosis and skewness; their models demonstrated that tumors with greater heterogeneity were associated with poor OS. Their datasets predicted OS with a concordance index of 0.69 to 0.74. Data from Cozzi *et al*[23] corroborated the finding that higher heterogeneity

correlates with worse prognosis; they found that tumors with lower homogeneity and higher dissimilarity textural features were associated with worse OS. However, skewness and kurtosis were not associated with survival outcomes in their study.

Increasing heterogeneity has also been associated with poor prognosis, irrespective of the imaging modality. For example, Hyun *et al*[24] reported that intratumoral heterogeneity measured by positron emission tomography textural features in pancreatic cancer patients predicted 2-year OS with an area under the curve of up to 0.72 using entropy features. Although studies evaluating the relationship between tumor heterogeneity and prognosis in pancreatic cancer are limited, tumor heterogeneity in other types of cancer has been shown to increase the risk of tumor recurrence, metastasis, resistance to treatment, and death[25,26]. Our 3D texture analysis extracted values of kurtosis and entropy. However, these values did not correlate with OS, and this might be because of the differences in features extracted between 3D and 2D analyses.

Although our study and other studies assessing pancreatic and colorectal cancers[27-29] have shown that higher entropy correlates with better prognosis, several others have shown that higher entropy correlates with worse prognosis in various cancers. This variability in the current literature suggests that entropy should not be used to predict prognosis in pancreatic cancer without further exploration. In our study, 2D analysis showed that higher entropy correlated with better PFS and less residual tumor following treatment. Sandrasegaran *et al*[29] reported similar findings; they observed better median OS times in patients with tumors with high entropy. However, this did not reach statistical significance. Cassinotto *et al*[14] showed that higher entropy correlated with less perineural invasion in pancreatic cancer, with an odds ratio of 0.018, which can help explain the positive prognostic implications of high entropy.

Although entropy reflects tumor heterogeneity similarly to skewness and kurtosis, entropy correlated differently with OS and PFS in our study; higher entropy was correlated with better prognosis. Other studies have shown that high entropy is associated with prognosis, poor treatment response, and aggressiveness in colorectal, pulmonary, and central nervous system tumors[27,30-32]. Several factors might explain these results. Unlike skewness and kurtosis, entropy analyzes randomness in the gray levels rather than in the distribution of gray levels in a region of interest[33]. Furthermore, tumor biology differs substantially among different organs, so what holds true in other organs may not be the same for the pancreas.

Additionally, entropy is prone to alterations in processing and image acquisition because entropy is area-dependent, whereby any region of interest covering less than 200 pixels can lead to the inaccurate estimation of entropy's relationship with any variable[34,35]. TexRad estimates entropy based on Shannon's model, the most straightforward and earliest model for estimating entropy. Still, TexRad might overestimate entropy by assuming that the pixels within a region of interest have an identical distribution and are entirely independent of neighboring pixels[34,36]. Given the insufficient data about the prognostic implications of entropy for pancreatic cancers, further studies are required to accurately assess the prognostic impact of entropy.

Our study has several strengths. Because all images were obtained on the same scanner, any heterogeneity in the results that may arise from using different scanners has been ruled out. Additionally, most studies using radiomics to evaluate response to treatment usually use delta radiomics to compare pretreatment and post-treatment scans. For example, Nasief *et al*[37] demonstrated that delta-radiomic features obtained during treatment periods could distinguish poor responders from good responders with an area under the curve of 0.94. Our pretreatment findings allow identifying patients who are more likely to respond before any treatment using baseline imaging, allowing for treatment selection that minimizes morbidity and thus limits expenses. This contrasts delta radiomics, which evaluates response after treatment has begun. Another strength of our study is comparing 2D and 3D analysis using TexRad and MIM software, respectively. It is well known that radiomics depend on how they are processed, and the software used[38,39]. However, our comparison showed that tumor density (mean HU) is a consistent and valid predictor of OS and PFS, irrespective of the type of analysis used.

Our study has some limitations. Our sample size was small, and it was a retrospective study. Therefore, more extensive prospective studies are needed to validate our findings. Additionally, CT acquisition factors might affect texture analysis variables; however, the effect is minimal. Lastly, our results were not externally validated and can only be directly applied to clinical practice with further validation.

CONCLUSION

In conclusion, tumor density (mean HU) was the only variable in our study that could reliably predict OS and PFS, irrespective of the type of analysis used. This variable may be used as a prognostic indicator to differentiate high-risk patients from low-risk patients and could be used for treatment planning. However, prospective studies will be beneficial to validate our findings externally.

ARTICLE HIGHLIGHTS

Research background

Radiomics can determine prognostic factors of several types of tumors.

Research motivation
Lack of evidence supporting radiomic studies on pancreatic cancer.

Research objectives
Compare two different radiomic softwares in assessing survival outcomes in pancreatic cancer patients.

Research methods
Retrospective review of pretreatment dual energy computed tomography (CT) images of 48 patients with biopsy confirmed lesions. Tumors were segmented using TexRad [2-dimensional (2D)] analysis software and MIM (3D) analysis software and radiomic features were extracted to compare with overall surgical (OS) and progression free survival (PFS).

Research results
3D analysis demonstrates that higher mean tumor density and median tumor density correlated with better OS, while 2D analysis showed that higher mean tumor density and mean positive pixels correlated with better OS. 2D analysis also showed higher skewness and kurtosis correlated with worse OS. Higher entropy correlated with better PFS. Patients with increased tumor size greater than 1.35 cm were likely to have a higher percentage of residual tumor above 10%.

Research conclusions
Radiomic features can serve as prognosis tools for pancreatic cancer and determine OS.

Research perspectives
This study serves as a guide for future research that can be verified through a prospective approach, while also contributing to possible alternatives to determine prognosis in patients using radiomic features.

ACKNOWLEDGEMENTS

We thank Erica Goodoff, Senior Scientific Editor in the Research Medical Library at The University of Texas MD Anderson Cancer Center, for editing this article.

FOOTNOTES

Author contributions: Saleh M, Virarkar M, Mahmoud HS, Wong VK, Gonzalez Baerga CI, Parikh M, Elsherif SB, and Bhosale PR have equally contributed to this paper with conception and design of the study, literature review and analysis, drafting and critical revision and editing, and final approval of the final version.

Institutional review board statement: The study was reviewed and approved by the University of Texas MD Anderson Cancer Center Institutional Review Board (approval No. 4 IRB00005015).

Informed consent statement: The informed consent was waived by the University of Texas MD Anderson Cancer Center Institutional Review Board.

Conflict-of-interest statement: All the authors report no relevant conflicts of interest for this article.

Data sharing statement: No additional data are available.

Country/Territory of origin: United States

ORCID number: Mayur Virarkar 0000-0002-5825-3102; Carlos Ignacio Gonzalez Baerga 0009-0008-9487-8303; Priya R Bhosale 0000-0003-4014-4941.

S-Editor: Wang JJ
L-Editor: A
P-Editor: Wang JJ

REFERENCES

1 **Siegel RL**, Miller KD, Jemal A. Cancer statistics, 2019. *CA Cancer J Clin* 2019; **69**: 7-34 [PMID: 30620402 DOI: 10.3322/caac.21551]

2 **Malla M**, Fekrmandi F, Malik N, Hatoum H, George S, Goldberg RM, Mukherjee S. The evolving role of radiation in pancreatic cancer. *Front Oncol* 2022; **12**: 1060885 [PMID: 36713520 DOI: 10.3389/fonc.2022.1060885]

3 **Krishnan S**, Chadha AS, Suh Y, Chen HC, Rao A, Das P, Minsky BD, Mahmood U, Delclos ME, Sawakuchi GO, Beddar S, Katz MH, Fleming JB, Javle MM, Varadhachary GR, Wolff RA, Crane CH. Focal Radiation Therapy Dose Escalation Improves Overall Survival in Locally Advanced Pancreatic Cancer Patients Receiving Induction Chemotherapy and Consolidative Chemoradiation. *Int J Radiat Oncol Biol Phys* 2016; **94**: 755-765 [PMID: 26972648 DOI: 10.1016/j.ijrobp.2015.12.003]

4 **Griffin JF**, Smalley SR, Jewell W, Paradelo JC, Reymond RD, Hassanein RE, Evans RG. Patterns of failure after curative resection of pancreatic carcinoma. *Cancer* 1990; **66**: 56-61 [PMID: 2354408 DOI: 10.1002/1097-0142(19900701)66:1<56::aid-cncr2820660112>3.0.co;2-6]

5 **Brody JR**, Costantino CL, Potoczek M, Cozzitorto J, McCue P, Yeo CJ, Hruban RH, Witkiewicz AK. Adenosquamous carcinoma of the pancreas harbors KRAS2, DPC4 and TP53 molecular alterations similar to pancreatic ductal adenocarcinoma. *Mod Pathol* 2009; **22**: 651-659 [PMID: 19270646 DOI: 10.1038/modpathol.2009.15]

6 **Dell'Aquila E**, Fulgenzi CAM, Minelli A, Citarella F, Stellato M, Pantano F, Russano M, Cursano MC, Napolitano A, Zeppola T, Vincenzi B, Tonini G, Santini D. Prognostic and predictive factors in pancreatic cancer. *Oncotarget* 2020; **11**: 924-941 [PMID: 32206189 DOI: 10.18632/oncotarget.27518]

7 **Hosny A**, Parmar C, Coroller TP, Grossmann P, Zeleznik R, Kumar A, Bussink J, Gillies RJ, Mak RH, Aerts HJWL. Deep learning for lung cancer prognostication: A retrospective multi-cohort radiomics study. *PLoS Med* 2018; **15**: e1002711 [PMID: 30500819 DOI: 10.1371/journal.pmed.1002711]

8 **Wu S**, Zheng J, Li Y, Yu H, Shi S, Xie W, Liu H, Su Y, Huang J, Lin T. A Radiomics Nomogram for the Preoperative Prediction of Lymph Node Metastasis in Bladder Cancer. *Clin Cancer Res* 2017; **23**: 6904-6911 [PMID: 28874414 DOI: 10.1158/1078-0432.CCR-17-1510]

9 **Horvat N**, Veeraraghavan H, Khan M, Blazic I, Zheng J, Capanu M, Sala E, Garcia-Aguilar J, Gollub MJ, Petkovska I. MR Imaging of Rectal Cancer: Radiomics Analysis to Assess Treatment Response after Neoadjuvant Therapy. *Radiology* 2018; **287**: 833-843 [PMID: 29514017 DOI: 10.1148/radiol.2018172300]

10 **Tang TY**, Li X, Zhang Q, Guo CX, Zhang XZ, Lao MY, Shen YN, Xiao WB, Ying SH, Sun K, Yu RS, Gao SL, Que RS, Chen W, Huang DB, Pang PP, Bai XL, Liang TB. Development of a Novel Multiparametric MRI Radiomic Nomogram for Preoperative Evaluation of Early Recurrence in Resectable Pancreatic Cancer. *J Magn Reson Imaging* 2020; **52**: 231-245 [PMID: 31867839 DOI: 10.1002/jmri.27024]

11 **Nasief H**, Zheng C, Schott D, Hall W, Tsai S, Erickson B, Allen Li X. A machine learning based delta-radiomics process for early prediction of treatment response of pancreatic cancer. *NPJ Precis Oncol* 2019; **3**: 25 [PMID: 31602401 DOI: 10.1038/s41698-019-0096-z]

12 **Zhang Y**, Lobo-Mueller EM, Karanicolas P, Gallinger S, Haider MA, Khalvati F. Prognostic Value of Transfer Learning Based Features in Resectable Pancreatic Ductal Adenocarcinoma. *Front Artif Intell* 2020; **3**: 550890 [PMID: 33733206 DOI: 10.3389/frai.2020.550890]

13 **Chakraborty J**, Midya A, Gazit L, Attiyeh M, Langdon-Embry L, Allen PJ, Do RKG, Simpson AL. CT radiomics to predict high-risk intraductal papillary mucinous neoplasms of the pancreas. *Med Phys* 2018; **45**: 5019-5029 [PMID: 30176047 DOI: 10.1002/mp.13159]

14 **Cassinotto C**, Chong J, Zogopoulos G, Reinhold C, Chiche L, Lafourcade JP, Cuggia A, Terrebonne E, Dohan A, Gallix B. Resectable pancreatic adenocarcinoma: Role of CT quantitative imaging biomarkers for predicting pathology and patient outcomes. *Eur J Radiol* 2017; **90**: 152-158 [PMID: 28583627 DOI: 10.1016/j.ejrad.2017.02.033]

15 **Fukukura Y**, Takumi K, Higashi M, Shinchi H, Kamimura K, Yoneyama T, Tateyama A. Contrast-enhanced CT and diffusion-weighted MR imaging: performance as a prognostic factor in patients with pancreatic ductal adenocarcinoma. *Eur J Radiol* 2014; **83**: 612-619 [PMID: 24418286 DOI: 10.1016/j.ejrad.2013.12.016]

16 **Zhu L**, Shi X, Xue H, Wu H, Chen G, Sun H, He Y, Jin Z, Liang Z, Zhang Z. CT Imaging Biomarkers Predict Clinical Outcomes After Pancreatic Cancer Surgery. *Medicine (Baltimore)* 2016; **95**: e2664 [PMID: 26844495 DOI: 10.1097/MD.0000000000002664]

17 **Kong B**, Cheng T, Wu W, Regel I, Raulefs S, Friess H, Erkan M, Esposito I, Kleeff J, Michalski CW. Hypoxia-induced endoplasmic reticulum stress characterizes a necrotic phenotype of pancreatic cancer. *Oncotarget* 2015; **6**: 32154-32160 [PMID: 26452217 DOI: 10.18632/oncotarget.5168]

18 **Hattori Y**, Gabata T, Zen Y, Mochizuki K, Kitagawa H, Matsui O. Poorly enhanced areas of pancreatic adenocarcinomas on late-phase dynamic computed tomography: comparison with pathological findings. *Pancreas* 2010; **39**: 1263-1270 [PMID: 20467344 DOI: 10.1097/MPA.0b013e3181dbc583]

19 **White RR**, Xie HB, Gottfried MR, Czito BG, Hurwitz HI, Morse MA, Blobe GC, Paulson EK, Baillie J, Branch MS, Jowell PS, Clary BM, Pappas TN, Tyler DS. Significance of histological response to preoperative chemoradiotherapy for pancreatic cancer. *Ann Surg Oncol* 2005; **12**: 214-221 [PMID: 15827813 DOI: 10.1245/ASO.2005.03.105]

20 **Chatterjee D**, Katz MH, Rashid A, Varadhachary GR, Wolff RA, Wang H, Lee JE, Pisters PW, Vauthey JN, Crane C, Gomez HF, Abbruzzese JL, Fleming JB. Histologic grading of the extent of residual carcinoma following neoadjuvant chemoradiation in pancreatic ductal adenocarcinoma: a predictor for patient outcome. *Cancer* 2012; **118**: 3182-3190 [PMID: 22028089 DOI: 10.1002/cncr.26651]

21 **Okubo S**, Kojima M, Matsuda Y, Hioki M, Shimizu Y, Toyama H, Morinaga S, Gotohda N, Uesaka K, Ishii G, Mino-Kenudson M, Takahashi S. Area of residual tumor (ART) can predict prognosis after post neoadjuvant therapy resection for pancreatic ductal adenocarcinoma. *Sci Rep* 2019; **9**: 17145 [PMID: 31748528 DOI: 10.1038/s41598-019-53801-2]

22 **Attiyeh MA**, Chakraborty J, Doussot A, Langdon-Embry L, Mainarich S, Gönen M, Balachandran VP, D'Angelica MI, DeMatteo RP, Jarnagin WR, Kingham TP, Allen PJ, Simpson AL, Do RK. Survival Prediction in Pancreatic Ductal Adenocarcinoma by Quantitative Computed Tomography Image Analysis. *Ann Surg Oncol* 2018; **25**: 1034-1042 [PMID: 29380093 DOI: 10.1245/s10434-017-6323-3]

23 **Cozzi L**, Comito T, Fogliata A, Franzese C, Franceschini D, Bonifacio C, Tozzi A, Di Brina L, Clerici E, Tomatis S, Reggiori G, Lobefalo F, Stravato A, Mancosu P, Zerbi A, Sollini M, Kirienko M, Chiti A, Scorsetti M. Computed tomography based radiomic signature as predictive of survival and local control after stereotactic body radiation therapy in pancreatic carcinoma. *PLoS One* 2019; **14**: e0210758 [PMID: 30657785 DOI: 10.1371/journal.pone.0210758]

24 **Hyun SH**, Kim HS, Choi SH, Choi DW, Lee JK, Lee KH, Park JO, Kim BT, Choi JY. Intratumoral heterogeneity of (18)F-FDG uptake predicts survival in patients with pancreatic ductal adenocarcinoma. *Eur J Nucl Med Mol Imaging* 2016; **43**: 1461-1468 [PMID: 26872788 DOI: 10.1007/s00259-016-3316-6]

25 **Verbeke C**. Morphological heterogeneity in ductal adenocarcinoma of the pancreas - Does it matter? *Pancreatology* 2016; **16**: 295-301 [PMID:

26924665 DOI: 10.1016/j.pan.2016.02.004]

26 **Bandyopadhyay S**, Basturk O, Coban I, Thirabanjasak D, Liang H, Altinel D, Adsay NV. Isolated solitary ducts (naked ducts) in adipose tissue: a specific but underappreciated finding of pancreatic adenocarcinoma and one of the potential reasons of understaging and high recurrence rate. *Am J Surg Pathol* 2009; **33**: 425-429 [PMID: 19092633 DOI: 10.1097/PAS.0b013e3181908e42]

27 **Ng F**, Ganeshan B, Kozarski R, Miles KA, Goh V. Assessment of primary colorectal cancer heterogeneity by using whole-tumor texture analysis: contrast-enhanced CT texture as a biomarker of 5-year survival. *Radiology* 2013; **266**: 177-184 [PMID: 23151829 DOI: 10.1148/radiol.12120254]

28 **Lubner MG**, Stabo N, Lubner SJ, del Rio AM, Song C, Halberg RB, Pickhardt PJ. CT textural analysis of hepatic metastatic colorectal cancer: pre-treatment tumor heterogeneity correlates with pathology and clinical outcomes. *Abdom Imaging* 2015; **40**: 2331-2337 [PMID: 25968046 DOI: 10.1007/s00261-015-0438-4]

29 **Sandrasegaran K**, Lin Y, Asare-Sawiri M, Taiyini T, Tann M. CT texture analysis of pancreatic cancer. *Eur Radiol* 2019; **29**: 1067-1073 [PMID: 30116961 DOI: 10.1007/s00330-018-5662-1]

30 **Chee CG**, Kim YH, Lee KH, Lee YJ, Park JH, Lee HS, Ahn S, Kim B. CT texture analysis in patients with locally advanced rectal cancer treated with neoadjuvant chemoradiotherapy: A potential imaging biomarker for treatment response and prognosis. *PLoS One* 2017; **12**: e0182883 [PMID: 28797063 DOI: 10.1371/journal.pone.0182883]

31 **Zhao Q**, Shi CZ, Luo LP. Role of the texture features of images in the diagnosis of solitary pulmonary nodules in different sizes. *Chin J Cancer Res* 2014; **26**: 451-458 [PMID: 25232219 DOI: 10.3978/j.issn.1000-9604.2014.08.07]

32 **Ryu YJ**, Choi SH, Park SJ, Yun TJ, Kim JH, Sohn CH. Glioma: application of whole-tumor texture analysis of diffusion-weighted imaging for the evaluation of tumor heterogeneity. *PLoS One* 2014; **9**: e108335 [PMID: 25268588 DOI: 10.1371/journal.pone.0108335]

33 **Guan Y**, Li W, Jiang Z, Chen Y, Liu S, He J, Zhou Z, Ge Y. Whole-Lesion Apparent Diffusion Coefficient-Based Entropy-Related Parameters for Characterizing Cervical Cancers: Initial Findings. *Acad Radiol* 2016; **23**: 1559-1567 [PMID: 27665235 DOI: 10.1016/j.acra.2016.08.010]

34 **Dercle L**, Ammari S, Bateson M, Durand PB, Haspinger E, Massard C, Jaudet C, Varga A, Deutsch E, Soria JC, Ferté C. Limits of radiomic-based entropy as a surrogate of tumor heterogeneity: ROI-area, acquisition protocol and tissue site exert substantial influence. *Sci Rep* 2017; **7**: 7952 [PMID: 28801575 DOI: 10.1038/s41598-017-08310-5]

35 **Shannon CE**. A Mathematical Theory of Communication. New York: Nokia Bell Labs, 1948; 27: 379-423

36 **Razlighi QR**, Kehtarnavaz N, Nosratinia A. Computation of image spatial entropy using quadrilateral Markov random field. *IEEE Trans Image Process* 2009; **18**: 2629-2639 [PMID: 19674952 DOI: 10.1109/TIP.2009.2029988]

37 **Nasief H**, Hall W, Zheng C, Tsai S, Wang L, Erickson B, Li XA. Improving Treatment Response Prediction for Chemoradiation Therapy of Pancreatic Cancer Using a Combination of Delta-Radiomics and the Clinical Biomarker CA19-9. *Front Oncol* 2019; **9**: 1464 [PMID: 31970088 DOI: 10.3389/fonc.2019.01464]

38 **Defeudis A**, De Mattia C, Rizzetto F, Calderoni F, Mazzetti S, Torresin A, Vanzulli A, Regge D, Giannini V. Standardization of CT radiomics features for multi-center analysis: impact of software settings and parameters. *Phys Med Biol* 2020; **65**: 195012 [PMID: 32575082 DOI: 10.1088/1361-6560/ab9f61]

39 **Foy JJ**, Robinson KR, Li H, Giger ML, Al-Hallaq H, Armato SG 3rd. Variation in algorithm implementation across radiomics software. *J Med Imaging (Bellingham)* 2018; **5**: 044505 [PMID: 30840747 DOI: 10.1117/1.JMI.5.4.044505]

World Journal of Radiology

Submit a Manuscript: https://www.f6publishing.com

World J Radiol 2023 November 28; 15(11): 315-323

DOI: 10.4329/wjr.v15.i11.315

ISSN 1949-8470 (online)

ORIGINAL ARTICLE

Basic Study

Imaging assessment of photosensitizer emission induced by radionuclide-derived Cherenkov radiation using charge-coupled device optical imaging and long-pass filters

Winn Aung, Atsushi B Tsuji, Kazuaki Rikiyama, Fumihiko Nishikido, Satoshi Obara, Tatsuya Higashi

Specialty type: Radiology, nuclear medicine and medical imaging

Provenance and peer review: Unsolicited article; Externally peer reviewed.

Peer-review model: Single blind

Peer-review report's scientific quality classification

Grade A (Excellent): 0
Grade B (Very good): B
Grade C (Good): 0
Grade D (Fair): 0
Grade E (Poor): 0

P-Reviewer: Zhou J, China

Received: October 3, 2023
Peer-review started: October 3, 2023
First decision: October 17, 2023
Revised: October 26, 2023
Accepted: November 17, 2023
Article in press: November 17, 2023
Published online: November 28, 2023

Winn Aung, Atsushi B Tsuji, Kazuaki Rikiyama, Satoshi Obara, Tatsuya Higashi, Department of Molecular Imaging and Theranostics, Institute for Quantum Medical Science, National Institutes for Quantum Science and Technology, Chiba 263-8555, Japan

Fumihiko Nishikido, Department of Advanced Nuclear Medicine Sciences, Institute for Quantum Medical Science, National Institutes for Quantum Science and Technology, Chiba 263-8555, Japan

Corresponding author: Winn Aung, MBBS, PhD, Senior Researcher, Department of Molecular Imaging and Theranostics, Institute for Quantum Medical Science, National Institutes for Quantum Science and Technology, 4-9-1 Anagawa, Inage-ku, Chiba 263-8555, Japan.
winn.aung@qst.go.jp

Abstract

BACKGROUND

Radionuclides produce Cherenkov radiation (CR), which can potentially activate photosensitizers (PSs) in phototherapy. Several groups have studied Cherenkov energy transfer to PSs using optical imaging; however, cost-effectively identifying whether PSs are excited by radionuclide-derived CR and detecting fluorescence emission from excited PSs remain a challenge. Many laboratories face the need for expensive dedicated equipment.

AIM

To cost-effectively confirm whether PSs are excited by radionuclide-derived CR and distinguish fluorescence emission from excited PSs.

METHODS

The absorbance and fluorescence spectra of PSs were measured using a micro-plate reader and fluorescence spectrometer to examine the photo-physical properties of PSs. To mitigate the need for expensive dedicated equipment and achieve the aim of the study, we developed a method that utilizes a charge-coupled device optical imaging system and appropriate long-pass filters of different wavelengths (manual sequential application of long-pass filters of 515, 580, 645, 700, 750, and 800 nm). Tetrakis (4-carboxyphenyl) porphyrin (TCPP) was utilized as a model PS. Different doses of copper-64 ($^{64}CuCl_2$) (4, 2, and 1 mCi) were used as CR-producing radionuclides. Imaging and data acquisition were

performed 0.5 h after sample preparation. Differential image analysis was conducted by using ImageJ software (National Institutes of Health) to visually evaluate TCPP fluorescence.

RESULTS

The maximum absorbance of TCPP was at 390–430 nm, and the emission peak was at 670 nm. The CR and CR-induced TCPP emissions were observed using the optical imaging system and the high-transmittance long-pass filters described above. The emission spectra of TCPP with a peak in the 645–700 nm window were obtained by calculation and subtraction based on the serial signal intensity (total flux) difference between $^{64}CuCl_2$ + TCPP and $^{64}CuCl_2$. Moreover, the differential fluorescence images of TCPP were obtained by subtracting the $^{64}CuCl_2$ image from the $^{64}CuCl_2$ + TCPP image. The experimental results considering different $^{64}CuCl_2$ doses showed a dose-dependent trend. These results demonstrate that a bioluminescence imaging device coupled with different long-pass filters and subtraction image processing can confirm the emission spectra and differential fluorescence images of CR-induced TCPP.

CONCLUSION

This simple method identifies the PS fluorescence emission generated by radionuclide-derived CR and can contribute to accelerating the development of Cherenkov energy transfer imaging and the discovery of new PSs.

Key Words: Tetrakis (4-carboxyphenyl) porphyrin; Photosensitizer emission; Radionuclide; Cherenkov radiation; Optical imaging; Long-pass filters

Core Tip: Radionuclides produce Cherenkov radiation (CR), which can potentially activate photosensitizers (PSs) in phototherapy. However, a cost-effective method to determine whether radionuclide-derived CR excites PSs and the measurement of fluorescence emitted by excited PS remain elusive. We propose a cost-effective method using a charge-coupled device optical imaging system combined with long-pass filters and subtraction image processing to distinguish CR and PS fluorescence emission. As a proof-of-concept, $^{64}CuCl_2$ and the PS tetrakis (4-carboxyphenyl) porphyrin were used in the experiments. This method can contribute to accelerating the development of Cherenkov energy transfer imaging and the discovery of new PSs.

Citation: Aung W, Tsuji AB, Rikiyama K, Nishikido F, Obara S, Higashi T. Imaging assessment of photosensitizer emission induced by radionuclide-derived Cherenkov radiation using charge-coupled device optical imaging and long-pass filters. *World J Radiol* 2023; 15(11): 315-323

URL: https://www.wjgnet.com/1949-8470/full/v15/i11/315.htm

DOI: https://dx.doi.org/10.4329/wjr.v15.i11.315

INTRODUCTION

Cherenkov radiation (CR) is the emission of photons when a charged particle moves faster than the speed of light in a medium[1]. Various radionuclides produce Cherenkov optical emission[2], which can potentially activate photosensitizers (PSs). This comprehensive phenomenon is interesting for various applications, including phototherapy, because it overcomes the limitations of light penetration[3,4]. Various researchers have been investigating CR-induced photodynamic therapy using certain radioisotopes[5-8]. Unfortunately, the availability of suitable PSs is currently limited and more effective PSs are needed.

Recently, photons from CR emitted from common radioisotopes have been detected using a highly sensitive charge-coupled device (CCD) optical imaging system[9,10]. However, when the radionuclide and PS coexist, the broad and continuous spectrum of the Cherenkov optical emission overlaps with the PS emission spectrum, obscuring the latter. Confirming whether the CR excites the PS is challenging because the required dedicated optical imaging devices (with built-in filters) are expensive. A method for distinguishing the Cherenkov optical emission from the PS fluorescence without expensive, dedicated instruments would benefit laboratories.

We evaluate whether an optical imaging system based on a CCD camera and different long-pass filters (Figure 1) can effectively detect and separate the radionuclide-derived CR emission from the CR-induced PS fluorescence spectrum. We used commercially available tetrakis (4-carboxyphenyl) porphyrin (TCPP) as a model PS, which can be conjugated to nanomaterials and applied to antimicrobial and anticancer phototherapies[11,12]. Among the various types of PSs, porphyrin-based PSs are commonly used for phototherapy[13]. The beta-emitting isotope Copper-64 ($^{64}CuCl_2$; $T_{1/2}$ = 12.7 h; β^+, 0.653 MeV; β^-, 0.579 MeV) was employed as a CR-producing radionuclide. This is a simple and cost-effective method to determine whether the fluorescence emitted from the PS is effectively the result of excitation by CR from a radionuclide.

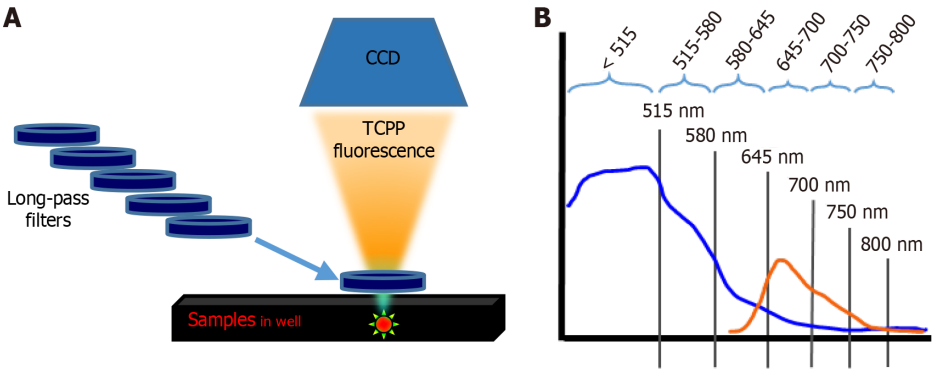

DOI: 10.4329/wjr.v15.i11.315 **Copyright** ©The Author(s) 2023.

Figure 1 Schematic diagram of the optical imaging approach used to detect Cherenkov optical emission and to separate the fluorescence emission of tetrakis (4-carboxyphenyl) porphyrin induced by Cherenkov optical emission. A: Long-pass filters step-cut the Cherenkov light, allowing the separation of tetrakis (4-carboxyphenyl) porphyrin (TCPP) emission; B: The Cherenkov light emitted from the radionuclide was gradually cut off with the appropriate long-pass filters of different wavelengths. The blue and orange curves are schematic representations of the Cherenkov optical emission and TCPP fluorescence spectra, respectively. CCD: Charge-coupled device optical imaging system.

MATERIALS AND METHODS

Materials

TCPP (molecular weight: 790.79) was purchased from Tokyo Chemical Industry Co., Ltd. (TCI, Tokyo, Japan). The chemical structure of TCPP is shown in Figure 2A. Phosphate Buffer (PB) was purchased from Wako Pure Chemical Co. (WAKO, Osaka, Japan). The beta-emitting isotope $^{64}CuCl_2$ was synthesized and provided by the Institute's Department of Advanced Nuclear Medicine Sciences (Chiba, Japan).

Examination of photo-physical properties of TCPP

Aqueous solutions of 0.1 mol/L TCPP were prepared by dissolving TCPP powder in PB (pH 7.4). The TCPP sample (100 μmol/L) was transferred to a 96-well plate. A SpectraMax M5 microplate reader (Molecular Devices, LLC, San Jose, CA, United States) with an operating range of 300–850 nm in 10 nm increments was used to record the absorbance spectrum of the sample. The three-dimensional fluorescence spectrum of TCPP was acquired using a JASCO FP-6600 fluorescence spectrometer (JASCO, Tokyo, Japan) equipped with a xenon lamp. The fluorescence emission intensity (FI) was measured at excitation wavelengths ranging from 350 nm to 600 nm in 5 nm increments. The emission wavelengths were measured in the 350–850 nm range in 2 nm increments. These measurements enabled the maximum excitation and emission wavelengths of TCPP to be determined.

Measurement of the concentration-dependent TCPP fluorescence intensity

The concentration-dependent FI of TCPP was measured using an Infinite 200 PRO multimode microplate reader (Tecan Japan Co., Ltd., Kawasaki, Japan) by setting the excitation wavelength to 430 nm, emission wavelength to 670 nm, gain to 79, and by integrating for 20 μs. A series of different TCPP concentrations (5, 10, 15, 20, 25, 30, 35, 40, 45, 50, 55, 60, 65, 70, 75, and 80 μmol/L) in PB were used for FI measurements. For spectral analysis, low TCPP concentrations (5, 10, 15, 20, 25, and 30 μmol/L) were measured using a multimode microplate reader (Tecan) operating in the emission wavelength range of 500–850 nm in 2 nm increments. The acquired FI was plotted against the wavelength.

Imaging with the VISQUE fluorescence imaging device

To visualize the LED-induced fluorescence emission from TCPP, TCPP solutions (1 mmol/L and 100 μmol/L) were added to a Nunc™ Flat-Bottom Microplate (96-well, Black) (Thermo Fisher Scientific, Roskilde, Denmark) and imaged with the VISQUE InVivo Smart fluorescence imaging and analysis system (Vieworks Co., Ltd, Gyeonggi, Korea) using the following specific excitation and emission filter combinations: Blue light (390–490 nm) excitation and red light (690–740 nm) emission. Constant parameters (exposure time: 500 ms; binning: 1 × 1; light intensity: Middle; mode: Low gain) were set and used for imaging.

Detection of radionuclide-derived CR and TCPP emission induced by CR with IVIS optical imaging system

The TCPP (30 μmol/L) and radionuclide $^{64}CuCl_2$ (4 mCi) were prepared in a 96-well black microplate (Thermo Fisher Scientific). At 0.5 h after preparing the samples, the CR emitted from the radionuclide was visualized using a sensitive CCD camera equipped with an IVIS Lumina optical imaging system (PerkinElmer, Waltham, MA, United States). The luminescent imaging mode with fixed acquisition parameters [emission filter: Open; excitation filter: Block; exposure time: 2 min; binning: 4 × 4; F/Stop (f): 1; field of view (FOV): 5 cm] was used in all experiments. Images of the wells containing the samples were acquired first. The optical signal intensity [total flux (photon/s)] was measured in the regions of interests (ROIs) corresponding to the sample-containing wells, and one empty well was used for background subtraction. Moreover, several high-transmittance long-pass filters of different wavelengths (515, 580, 645, 700, 750, and

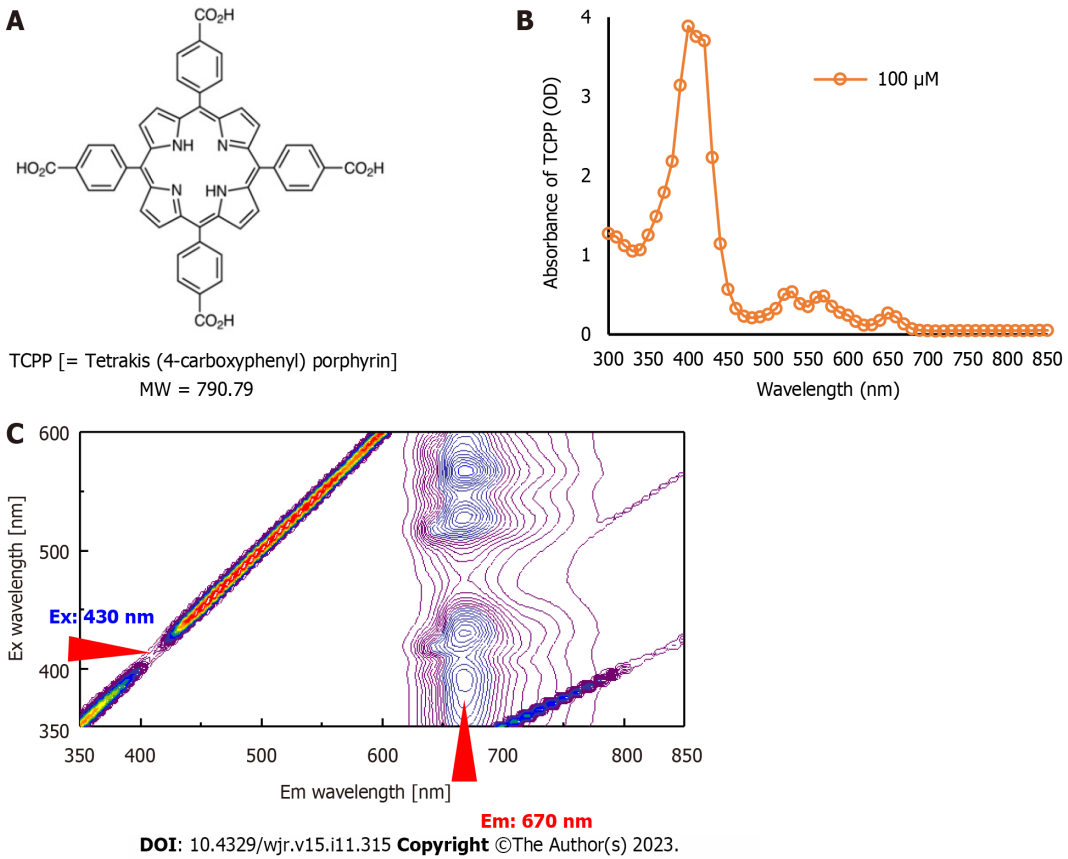

DOI: 10.4329/wjr.v15.i11.315 **Copyright** ©The Author(s) 2023.

Figure 2 Chemical structure and photo-physical properties of tetrakis (4-carboxyphenyl) porphyrin. A: Chemical structure of tetrakis (4-carboxyphenyl) porphyrin (TCPP); B: Absorption spectrum of TCPP (100 μmol/L) at 25°C in phosphate buffer; C: Three-dimensional fluorescence spectral analysis of TCPP. Fluorescence emission was observed around 670 nm with an excitation wavelength of 430 nm. Em: Emission wavelength; Ex: Excitation wavelength; MW: Molecular weight; μM: μmol/L.

800 nm) were used to separate the emission spectrum of TCPP and the Cherenkov light emitted by the radionuclide. A schematic of the experimental setup is shown in Figure 1. Each filter was manually placed on the wells, and images were acquired sequentially (Figure 1A). Image analysis was performed using Living Image 2.6 (PerkinElmer). First, the total flux of the wells containing samples was obtained by subtracting the total flux of the empty background. Subsequently, for each well, the total flux emitted within the window of the adjacent wavelengths of the two filters was calculated from the difference in the total flux measured with each respective filter (Figure 1B). For all pairs of wavelength windows, the total flux of $^{64}CuCl_2$ + TCPP and $^{64}CuCl_2$ was obtained by subtracting the total flux of the PB-filled wells. Second, the emission spectrum of TCPP was acquired by plotting the total flux difference between $^{64}CuCl_2$ + TCPP and $^{64}CuCl_2$ in the respective wavelength ranges. In addition, differential image analysis was performed to visually assess TCPP fluorescence by subtracting the $^{64}CuCl_2$ image from the $^{64}CuCl_2$ + TCPP image using ImageJ [https://imagej.nih.gov/ij/; National Institutes of Health (NIH), Bethesda, Maryland, United States][14]. The same experiment was also performed with 2 mCi and 1 mCi $^{64}CuCl_2$.

RESULTS

Absorbance and fluorescence spectra of TCPP

The peak of the TCPP absorbance spectrum was in the 390–430 nm range (Figure 2B). In the three-dimensional fluorescence spectral analysis, the peak emission of TCPP was approximately 670 nm with excitation wavelengths of 350–600 nm (Figure 2C). Among the excitation wavelengths, 430 nm was considered the peak excitation wavelength for TCPP because it induced the highest fluorescence emission from TCPP and approximately corresponded with the wavelength of the most intense CR peak.

Concentration-dependent TCPP fluorescence

The FI of TCPP (5–80 μmol/L) linearly correlated with concentrations up to approximately 30 μmol/L. Above 30 μmol/L, the FI slope decreased (Figure 3A). This is likely due to TCPP stacking in the samples. Therefore, only low TCPP concentrations (5–30 μmol/L) were used for fluorescence spectral analysis. We found that the 430 nm wavelength excited TCPP to fluoresce over a range of wavelengths (625–775 nm) with a peak at 670 nm (Figure 3B).

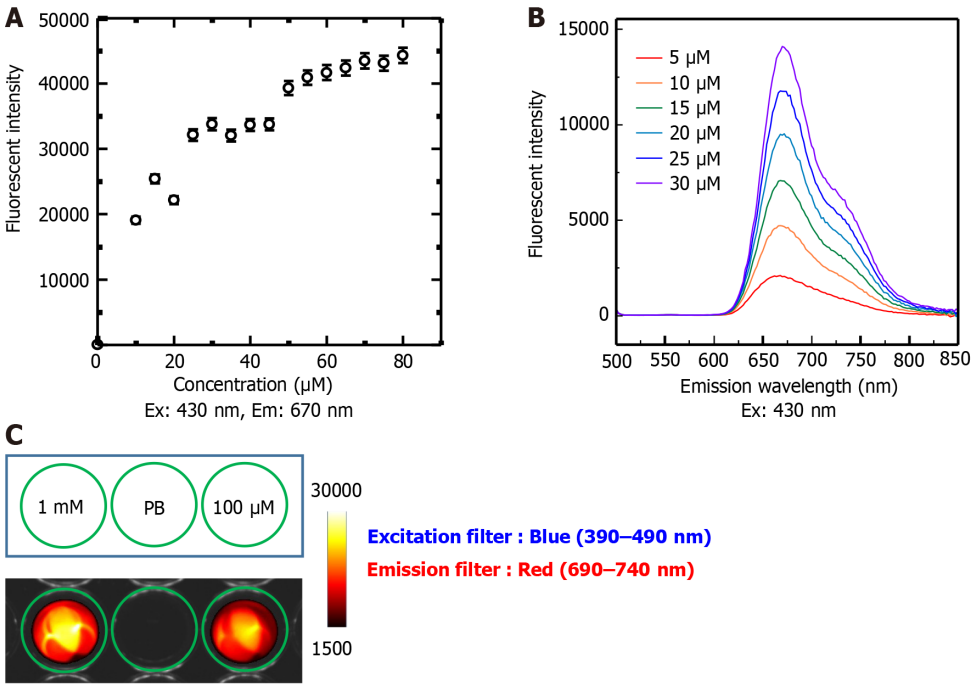

DOI: 10.4329/wjr.v15.i11.315

Figure 3 Tetrakis (4-carboxyphenyl) porphyrin fluorescence emission. A: Fluorescence emission intensity of tetrakis (4-carboxyphenyl) porphyrin (TCPP) prepared at different concentrations (5, 10, 15, 20, 25, 30, 35, 40, 45, 50, 55, 60, 65, 70, 75, and 80 μmol/L in PB) measured by setting the excitation wavelength to 430 nm and emission wavelength to 670 nm. The relationship is linear up to approximately 30 μmol/L; B: The fluorescence spectra of low TCPP concentrations (5, 10, 15, 20, 25, and 30 μmol/L) were measured with the excitation wavelength set to 430 nm; C: Visualization of TCPP fluorescence emission using a light-emitting diode light source, blue light excitation filter (390–490 nm), and red light emission filter (690–740 nm). Em: Emission wavelength; Ex: Excitation wavelength; mM: mmol/L; PB: Phosphate buffer; μM: μmol/L.

Imaging of TCPP with VISQUE imaging device

The inherent fluorescence characteristics of TCPP emission could be visualized and confirmed using a fluorescence imaging system with a light-emitting diode light source and a set of filters for blue light (390–490 nm) excitation and red light (690–740 nm) emission (Figure 3C). Both filters were compatible with the excitation/emission wavelengths of TCPP (430/670 nm).

Detection of CR and separation of CR-induced emission spectrum of TCPP

At 0.5 h after preparing the samples in the wells, images were acquired without a filter. Cherenkov luminescence from the radionuclide was detected in the two wells on the left containing $^{64}CuCl_2$ + TCPP and $^{64}CuCl_2$, respectively. In contrast, luminescence was not visualized in the two wells on the right containing either PB or TCPP (Figure 4A, upper row). The total flux produced from the light emission of the radionuclides decreased when the wells were covered with long-pass filters of different wavelengths. Serial application of long-pass filters of 515, 580, 645, 700, 750, and 800 nm resulted in a sequential decrease in total flux measured from the ROIs of wells with $^{64}CuCl_2$ only (Figure 4A, upper row, lower left well) and $^{64}CuCl_2$ + TCPP (Figure 4A, upper row, upper left well). The TCPP emission spectral band was separated using the following calculation. First, the total flux emitted from $^{64}CuCl_2$ + TCPP and $^{64}CuCl_2$ at two adjacent wavelengths was measured. Second, the optical signals for the serial pairs of the wavelength window were calculated based on the difference in the signals measured with each filter. Subsequently, the emission spectrum of TCPP was calculated by subtracting the total flux of $^{64}CuCl_2$ from that of $^{64}CuCl_2$ + TCPP. The resulting spectrum is shown in Figure 4. Using ImageJ software (NIH), differential image analysis was conducted by subtracting the $^{64}CuCl_2$ image from the $^{64}CuCl_2$ + TCPP image to visually evaluate TCPP fluorescence (Figure 4A, lower row). The spectral peaks with the maximum intensity were in the 645–700 nm window, marked by the red dotted rim in the lower row of Figure 4A and the line graph in Figure 4D. Similar results were obtained for the other two doses, 2 mCi (Figure 4B and D) and 1 mCi (Figure 4C and D). The total flux exhibited a dose-dependent tendency.

DISCUSSION

This study demonstrates that imaging with an optical imaging device coupled with different long-pass filters and subtraction image processing separates the spectra of CR and PS emissions, providing optical images of the emission from a PS at different wavelengths. Although distinguishing the Cherenkov light from the PS emission was difficult, the subtraction image processing effectively separated them. Thus, the combined use of a device set and image processing

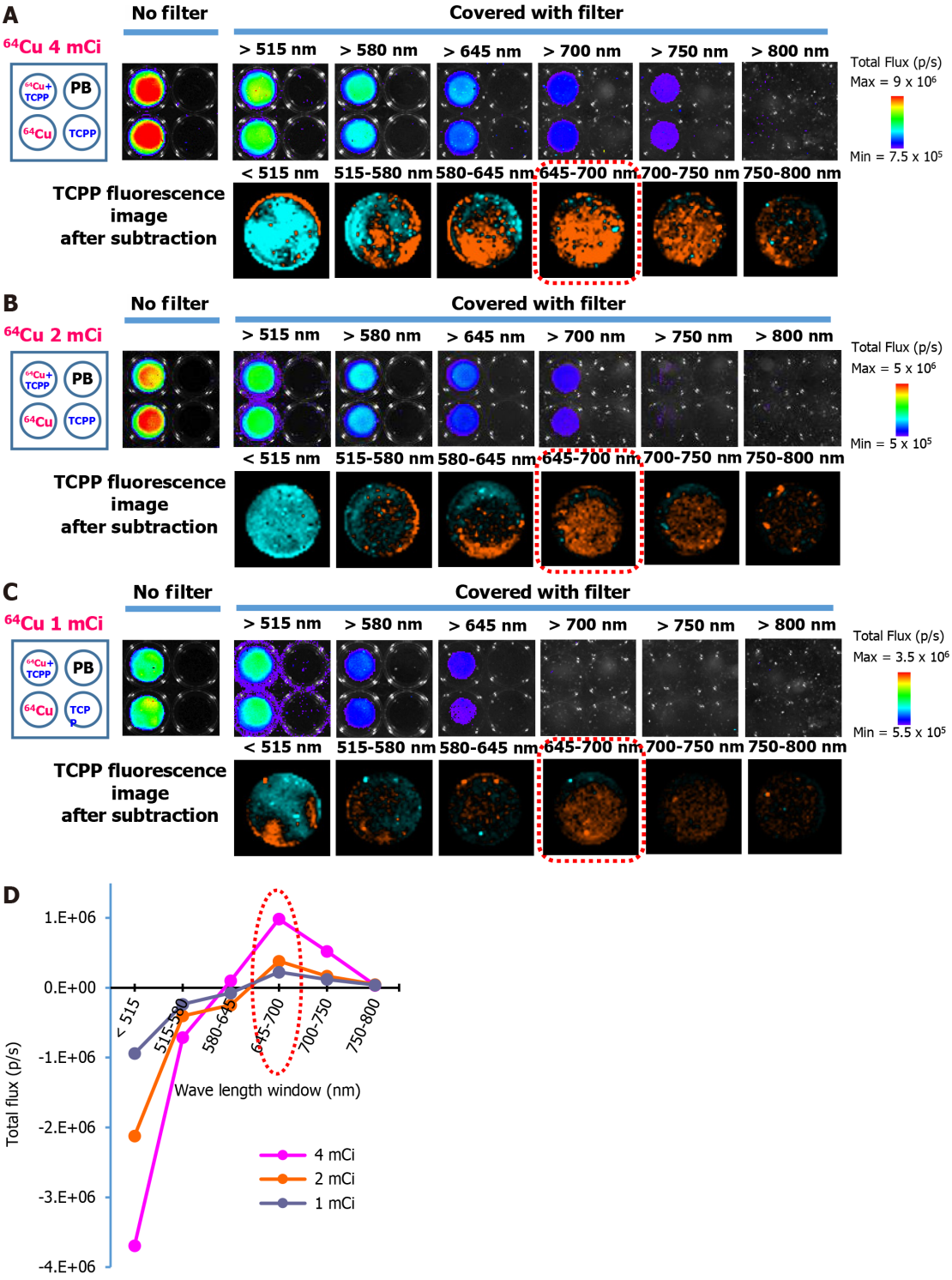

DOI: 10.4329/wjr.v15.i11.315

Figure 4 Detection of Cherenkov radiation and emission spectrum of tetrakis (4-carboxyphenyl) porphyrin induced by Cherenkov radiation. A: Bioluminescence imaging of prepared samples $^{64}CuCl_2$ (4 mCi) and $^{64}CuCl_2$ (4 mCi) + tetrakis (4-carboxyphenyl) porphyrin (TCPP) (30 μmol/L) with or without covering by long-pass filters (upper row), and TCPP fluorescence image after subtraction in differential image analysis (lower row); B: Similar images acquired from the experiment using $^{64}CuCl_2$ (2 mCi); C: Similar images acquired from the experiment using $^{64}CuCl_2$ (1 mCi); D: TCPP fluorescence spectrum calculated by subtracting the total flux of $^{64}CuCl_2$ from that of $^{64}CuCl_2$ + TCPP. The spectral peak was found in the 645–700 nm window. The peak is indicated by the red dotted circle. ^{64}Cu: $^{64}CuCl_2$; PB: Phosphate buffer; μM: μmol/L.

could be utilized in laboratories with optical imaging devices.

The three-dimensional fluorescence spectral analysis showed that TCPP was excited by light wavelengths from 350 nm to 600 nm, producing a large Stokes shift and an emission peak at approximately 670 nm. The CR spectrum was continuous, peaking at high frequencies (ultraviolet/blue)[15,16]. Therefore, the absorption profile of TCPP (390–430 nm) matched the Cherenkov emission profile.

A bioluminescence imaging device, an IVIS optical imaging system with six different long-pass filters, can provide various optical images of CR plus PS emission. Our lab has an IVIS imaging system and six long-pass filters that are not built into the device but used for other purposes. We manually placed each filter on the wells containing ^{64}Cu and PS and captured optical images (Figure 4A-C, upper rows). When the wells were covered with long-pass filters, the total flux derived from ^{64}Cu-containing wells decreased when the wavelength of the applied filters increased. This could occur because the wavelength of the filters exceeded the maximum emission peak of CR (350–500 nm) and cut off the Cherenkov light. Visually distinguishing the emission from $^{64}CuCl_2$ and $^{64}CuCl_2$ + TCPP is challenging, even though the TCPP emission spectrum can be calculated (Figure 4D). Thus, an additional process is required to visualize only the light emitted from the PS.

The PS emissions were distinguished from the CR emissions using image processing. The image data acquired by the IVIS system were processed using ImageJ, a simple and free software package provided by NIH, to obtain the differential image. The TCPP fluorescence image was easily generated by subtracting the $^{64}CuCl_2$ image from the $^{64}CuCl_2$ + TCPP image (Figure 4A-C, lower rows). These results displayed a dose-dependent trend. Moreover, both the TCPP fluorescence images (Figure 4A-C, lower rows) and spectra (Figure 4D) were consistent with the results obtained from the fluorescence spectral analysis of the TCPP (Figure 3B), showing a fluorescence peak at 645–700 nm.

Overall, the developed method could be used to compare different PSs and provide information to select the optimal PS. In addition, various laboratories with conventional optical imaging devices could easily apply this method when conducting studies. Some laboratories have appropriate long-pass filters, whereas others could obtain them inexpensively. The ImageJ software is available to all laboratories; however, only a few laboratories can currently screen for appropriate PSs for Cherenkov energy transfer imaging. The proposed method could enable more laboratories to perform these procedures, contributing to the accelerated development of Cherenkov energy transfer imaging for multiple applications. The main objective of this study was to demonstrate the feasibility of the proposed method as a proof of concept; however, the method would need to be more comprehensively tested to address possible limitations. First, the reproducibility would have to be determined and statistically assessed. Second, we evaluated only one PS, namely TCPP. Further studies would have to compare the results for different PSs. Third, we used only one radionuclide, $^{64}CuCl_2$. Other beta-emitting radioactive sources producing decay products with energies above the Cerenkov threshold (approximately 220 keV) could be employed in future studies[17]. The next step would therefore entail more detailed examinations.

CONCLUSION

A simple method using a CCD optical imaging system in combination with different high-transmission long-pass filters and subtraction image processing was capable of potentially evaluating whether PS candidates are reliably excited by radionuclide-derived CR to produce fluorescence emission. The widespread adoption of this method could be expected to contribute to the discovery of a range of new effective PSs.

ARTICLE HIGHLIGHTS

Research background

Cherenkov radiation (CR) is the emission of photons when a charged particle moves faster than the speed of light in a medium. Various radionuclides produce Cherenkov optical emission, which can potentially activate photosensitizers (PSs) in phototherapy.

Research motivation

Several researchers are investigating CR-induced photodynamic therapy using radioisotopes and Cherenkov energy transfer to PSs using optical imaging. However, the effective management of the process, particularly the cost-effective confirmation that a PS is excited by CR and identifying appropriate PSs, remains a challenge.

Research objectives

The purpose of this study is to propose a cost-effective method to determine whether the PS is excited by radionuclide-derived CR and to distinguish the fluorescence emission from PS excitation.

Research methods

Tetrakis (4-carboxyphenyl) porphyrin (TCPP) and Copper-64 ($^{64}CuCl_2$) were utilized as a model PS and a CR-producing radionuclide, respectively. The photo-physical properties (absorbance and fluorescence spectra) of TCPP were measured using a microplate reader and fluorescence spectrometer. Imaging and data acquisition were performed with a charge-coupled device optical imaging system and appropriate long-pass filters of different wavelengths. To visually evaluate the TCPP fluorescence, differential image analysis was conducted using ImageJ software (National Institutes of Health).

Research results

Optical imaging coupled with high-transmittance long-pass filters and subtraction image processing separated the

emission spectra of the radionuclide-derived CR and TCPP. The emission spectra of TCPP were obtained by calculation and subtraction based on the serial signal intensity (total flux) difference between $^{64}CuCl_2$ + TCPP and $^{64}CuCl_2$. In addition, the differential fluorescence images of TCPP were acquired by subtracting the $^{64}CuCl_2$ image from the $^{64}CuCl_2$ + TCPP image.

Research conclusions

This simple and cost-effective method could confirm the PS fluorescence emission generated by radionuclide-derived CR. Moreover, the method can contribute to accelerating the development of Cherenkov energy transfer imaging and the discovery of new effective PSs.

Research perspectives

Several laboratories with conventional optical imaging devices would be able to acquire suitable long-pass filters at low cost and easily apply this method to compare different PSs to identify the optimal PS. A potential limitation of this study, namely the use of limited experiments with only one PS and one radionuclide, could be addressed by conducting much more detailed examinations as the next step.

ACKNOWLEDGEMENTS

The authors thank the members of the Cyclotron Operation Section for providing ^{64}Cu. We are grateful to Osada Kensuke and Yamaya Taiga for their helpful discussions and suggestions.

FOOTNOTES

Author contributions: Aung W conceptualized and designed the study; Aung W, Rikiyama K and Nishikido F conducted the experiments and analyzed the data; Obara S performed the subtraction image processing; Aung W and Tsuji AB wrote the manuscript; Tsuji AB and Higashi T coordinated the research and contributed to manuscript preparation; all authors contributed to manuscript revision; All authors read and approved the final manuscript.

Supported by Grant-in-Aid for Scientific Research (C) from the Japan Society for the Promotion of Science, No. 21K07740.

Institutional review board statement: This study was reviewed and approved by the Institutional Review Board of National Institutes for Quantum Science and Technology, No. 07-1064-28. No animals or animal-derived samples or patients or patient-derived samples were included in this study.

Conflict-of-interest statement: The authors declare no potential conflicts of interest for this article.

Data sharing statement: All relevant data were presented in the manuscript. Further information is available from the corresponding author at winn.aung@qst.go.jp.

ARRIVE guidelines statement: The authors have read the ARRIVE guidelines, and the manuscript was prepared and revised according to the ARRIVE guidelines.

Country/Territory of origin: Japan

ORCID number: Winn Aung 0000-0002-0896-7158; Atsushi B Tsuji 0000-0003-2726-288X; Kazuaki Rikiyama 0000-0001-6474-535X; Fumihiko Nishikido 0000-0002-2952-281X; Satoshi Obara 0000-0002-2577-4243; Tatsuya Higashi 0000-0002-8338-4737.

Corresponding Author's Membership in Professional Societies: Japanese Society of Nuclear Medicine, No. 11047.

S-Editor: Lin C
L-Editor: Filipodia
P-Editor: Zhao S

REFERENCES

1 **Cherenkov PA**. Visible Light from Clear Liquids Under the Action of Gamma Radiation. *CR (Dokl) Acad Sci URSS* 1934; **2**: 451-454 [DOI: 10.3103/s1062873812120271]

2 **Ruggiero A**, Holland JP, Lewis JS, Grimm J. Cerenkov luminescence imaging of medical isotopes. *J Nucl Med* 2010; **51**: 1123-1130 [PMID: 20554722 DOI: 10.2967/jnumed.110.076521]

3 **Klein JS**, Sun C, Pratx G. Radioluminescence in biomedicine: physics, applications, and models. *Phys Med Biol* 2019; **64**: 04TR01 [PMID: 30524090 DOI: 10.1088/1361-6560/aaf4de]

4 **Ran C**, Zhang Z, Hooker J, Moore A. In vivo photoactivation without "light": use of Cherenkov radiation to overcome the penetration limit of light. *Mol Imaging Biol* 2012; **14**: 156-162 [PMID: 21538154 DOI: 10.1007/s11307-011-0489-z]

5 **Kotagiri N**, Sudlow GP, Akers WJ, Achilefu S. Breaking the depth dependency of phototherapy with Cerenkov radiation and low-radiance-responsive nanophotosensitizers. *Nat Nanotechnol* 2015; **10**: 370-379 [PMID: 25751304 DOI: 10.1038/nnano.2015.17]

6 **Hartl BA**, Hirschberg H, Marcu L, Cherry SR. Activating Photodynamic Therapy *in vitro* with Cerenkov Radiation Generated from Yttrium-90. *J Environ Pathol Toxicol Oncol* 2016; **35**: 185-192 [PMID: 27481495 DOI: 10.1615/JEnvironPatholToxicolOncol.2016016903]

7 **Kamkaew A**, Cheng L, Goel S, Valdovinos HF, Barnhart TE, Liu Z, Cai W. Cerenkov Radiation Induced Photodynamic Therapy Using Chlorin e6-Loaded Hollow Mesoporous Silica Nanoparticles. *ACS Appl Mater Interfaces* 2016; **8**: 26630-26637 [PMID: 27657487 DOI: 10.1021/acsami.6b10255]

8 **Guo R**, Jiang D, Gai Y, Qian R, Zhu Z, Gao Y, Jing B, Yang B, Lan X, An R. Chlorin e6-loaded goat milk-derived extracellular vesicles for Cerenkov luminescence-induced photodynamic therapy. *Eur J Nucl Med Mol Imaging* 2023; **50**: 508-524 [PMID: 36222853 DOI: 10.1007/s00259-022-05978-4]

9 **Robertson R**, Germanos MS, Li C, Mitchell GS, Cherry SR, Silva MD. Optical imaging of Cerenkov light generation from positron-emitting radiotracers. *Phys Med Biol* 2009; **54**: N355-N365 [PMID: 19636082 DOI: 10.1088/0031-9155/54/16/N01]

10 **Spinelli AE**, D'Ambrosio D, Calderan L, Marengo M, Sbarbati A, Boschi F. Cerenkov radiation allows *in vivo* optical imaging of positron emitting radiotracers. *Phys Med Biol* 2010; **55**: 483-495 [PMID: 20023328 DOI: 10.1088/0031-9155/55/2/010]

11 **Zhang Y**, Ma J, Wang D, Xu C, Sheng S, Cheng J, Bao C, Li Y, Tian H. Fe-TCPP@CS nanoparticles as photodynamic and photothermal agents for efficient antimicrobial therapy. *Biomater Sci* 2020; **8**: 6526-6532 [PMID: 33103167 DOI: 10.1039/d0bm01427c]

12 **Li B**, Wang X, Chen L, Zhou Y, Dang W, Chang J, Wu C. Ultrathin Cu-TCPP MOF nanosheets: a new theragnostic nanoplatform with magnetic resonance/near-infrared thermal imaging for synergistic phototherapy of cancers. *Theranostics* 2018; **8**: 4086-4096 [PMID: 30128038 DOI: 10.7150/thno.25433]

13 **Malatesti N**, Munitic I, Jurak I. Porphyrin-based cationic amphiphilic photosensitisers as potential anticancer, antimicrobial and immunosuppressive agents. *Biophys Rev* 2017; **9**: 149-168 [PMID: 28510089 DOI: 10.1007/s12551-017-0257-7]

14 **U. S. National Institutes of Health**. ImageJ. [cited 12 February 2023]. Available from: https://imagej.nih.gov/ij/

15 **Spinelli AE**, Boschi F. Novel biomedical applications of Cerenkov radiation and radioluminescence imaging. *Phys Med* 2015; **31**: 120-129 [PMID: 25555905 DOI: 10.1016/j.ejmp.2014.12.003]

16 **Dothager RS**, Goiffon RJ, Jackson E, Harpstrite S, Piwnica-Worms D. Cerenkov radiation energy transfer (CRET) imaging: a novel method for optical imaging of PET isotopes in biological systems. *PLoS One* 2010; **5**: e13300 [PMID: 20949021 DOI: 10.1371/journal.pone.0013300]

17 **Ciarrocchi E**, Belcari N. Cerenkov luminescence imaging: physics principles and potential applications in biomedical sciences. *EJNMMI Phys* 2017; **4**: 14 [PMID: 28283990 DOI: 10.1186/s40658-017-0181-8]

World Journal of Radiology

Submit a Manuscript: https://www.f6publishing.com

World J Radiol 2023 November 28; 15(11): 324-337

DOI: 10.4329/wjr.v15.i11.324

ISSN 1949-8470 (online)

META-ANALYSIS

Association between late gadolinium enhancement and outcome in dilated cardiomyopathy: A meta-analysis

Xin-Yi Feng, Wen-Feng He, Tian-Yue Zhang, Ling-Li Wang, Fan Yang, Yu-Ling Feng, Chun-Ping Li, Rui Li

Specialty type: Radiology, nuclear medicine and medical imaging

Provenance and peer review: Unsolicited article; Externally peer reviewed.

Peer-review model: Single blind

Peer-review report's scientific quality classification

Grade A (Excellent): 0
Grade B (Very good): 0
Grade C (Good): C
Grade D (Fair): 0
Grade E (Poor): 0

P-Reviewer: Barison A, Italy

Received: August 17, 2023
Peer-review started: August 17, 2023
First decision: September 14, 2023
Revised: September 29, 2023
Accepted: October 23, 2023
Article in press: October 23, 2023
Published online: November 28, 2023

Xin-Yi Feng, Tian-Yue Zhang, Ling-Li Wang, Fan Yang, Yu-Ling Feng, Chun-Ping Li, Rui Li, Department of Radiology, The Affiliated Hospital of North Sichuan Medical College, Nanchong 637000, Sichuan Province, China

Wen-Feng He, Department of Cardiology, The Affiliated Hospital of North Sichuan Medical College, Nanchong 637000, Sichuan Province, China

Corresponding author: Rui Li, PhD, Doctor, Department of Radiology, The Affiliated Hospital of North Sichuan Medical College, Maoyuan South Road, Shunqing District, Nanchong 637000, Sichuan Province, China. ddtwg_nsmc@163.com

Abstract

BACKGROUND

The prognostic value of late gadolinium enhancement (LGE) derived from cardiovascular magnetic resonance (CMR) is well studied, and several new metrics of LGE have emerged. However, some controversies remain; therefore, further discussion is needed, and more precise risk stratification should be explored.

AIM

To investigate the associations between the positivity, extent, location, and pattern of LGE and multiple outcomes in dilated cardiomyopathy (DCM).

METHODS

PubMed, Ovid MEDLINE, and Cochrane Library were searched for studies that investigated the prognostic value of LGE in patients with DCM. Pooled hazard ratios (HRs) and 95% confidence intervals were calculated to assess the role of LGE in the risk stratification of DCM.

RESULTS

Nineteen studies involving 7330 patients with DCM were included in this meta-analysis and covered a wide spectrum of DCM, with a mean left ventricular ejection fraction between 21% and 50%. The meta-analysis revealed that the presence of LGE was associated with an increased risk of multiple adverse outcomes (all-cause mortality, HR: 2.14; arrhythmic events, HR: 5.12; and composite endpoints, HR: 2.38; all $P < 0.001$). Furthermore, every 1% increment in the extent of LGE was associated with an increased risk of all-cause mortality. Analysis of a subgroup revealed that the prognostic value varied based on different location and pattern of LGE. Additionally, we found that LGE was a

stronger predictor of arrhythmic events in patients with greater left ventricular ejection fraction.

CONCLUSION
LGE by CMR in patients with DCM exhibited a substantial value in predicting adverse outcomes, and the extent, location, and pattern of LGE could provide additional information for risk stratification.

Key Words: Cardiac magnetic resonance; Dilated cardiomyopathy; Late gadolinium enhancement; Meta-analysis; Myocardial fibrosis; Prognosis

Core Tip: The prognostic value of late gadolinium enhancement (LGE) is well studied, and several new metrics of LGE have emerged. However, some controversies remain; therefore, further discussion is needed, and a more precise risk stratification should be explored.

Citation: Feng XY, He WF, Zhang TY, Wang LL, Yang F, Feng YL, Li CP, Li R. Association between late gadolinium enhancement and outcome in dilated cardiomyopathy: A meta-analysis. *World J Radiol* 2023; 15(11): 324-337
URL: https://www.wjgnet.com/1949-8470/full/v15/i11/324.htm
DOI: https://dx.doi.org/10.4329/wjr.v15.i11.324

INTRODUCTION

Dilated cardiomyopathy (DCM) is a heterogeneous heart muscle disease with a prevalence of 1 in 2500 adults. Even with advances in therapy, the prognosis of patients with DCM remains poor (the 5-year mortality rate was as high as 20%) and varies considerably among individuals[1]. Therefore, prognostic stratification in DCM has become a demanding issue in clinical practice.

Currently, the left ventricular ejection fraction (LVEF) is a common applicable indicator for risk stratification in patients with DCM. However, the strategy of using the LVEF alone as a prognostic factor is inadequate in predicting adverse outcomes[2]. Occurring in approximately 30% of patients with DCM, myocardial scar is the most important underlying pathology of sudden cardiac death (SCD) events and the major substrate for ventricular arrhythmia. Late gadolinium enhancement (LGE) based on cardiovascular magnetic resonance (CMR) is currently the gold standard for evaluating localized myocardial fibrosis. Studies have confirmed that LGE is an independent and powerful predictor of adverse outcomes in DCM and could increase the prognostic value of LVEF[2-4].

However, most studies have focused on the presence of LGE and adverse outcomes. With the continuously developing research on LGE in patients with DCM, more studies have incorporated new indicators (the extent, location, and pattern of LGE) to assess the outcomes in patients with DCM, other than just the presence of LGE. Therefore, this meta-analysis was designed to evaluate the role of those novel indicators of LGE in the risk stratification of DCM.

MATERIALS AND METHODS

The network meta-analysis extension of the Preferred Reporting Items for Systematic Reviews and Meta-Analyses (PRISMA-NMA) guidelines provided support in guiding this review[5].

Data sources and search strategy

The following databases were searched according to the methods recommended by the Cochrane Handbook: PubMed, Ovid MEDLINE, and Cochrane Library. Studies were searched using relevant controlled vocabulary thesauruses (Medical Subject Headings terms for PubMed) and synonyms for these terms: "dilated cardiomyopathy," "cardiac magnetic resonance," "late gadolinium enhancement," and "prognosis." The details of the search strategy adopted for PubMed, Ovid MEDLINE, and the Cochrane Library are shown in the Appendix. These searches were limited to cohort studies and were finalized in December 2021.

Eligibility criteria and outcomes

Observational cohort studies, both prospective and retrospective, were included in the meta-analysis if they reported the prognostic value of LGE in DCM and specified the exclusion of ischemic heart disease (*i.e.*, any medical documentation (coronary angiography, myocardial perfusion imaging, or medical records) that indicated the presence of ischemic heart disease and significant coronary artery disease); moreover, studies with transmural LGE without any history of coronary artery disease or myocardial infarction were included if the imaging phenotype including LGE distribution was not coherent with an ischemic insult in a specific coronary artery territory. When the population of a study also included

patients with cardiomyopathies other than DCM, only those with DCM were considered for the meta-analysis. Furthermore, only studies that quantified the extent of LGE as a percentage of left ventricular mass were included in the meta-analysis. The endpoints were classified into three subgroups: (1) All-cause mortality; (2) arrhythmic events, including SCD, cardiac arrest due to ventricular fibrillation (VF), sustained ventricular tachycardia (VT), or appropriate implantable cardioverter–defibrillator (ICD) intervention; and (3) composite endpoints, including all-cause mortality and cardiac events. Cardiac events, included cardiac death[2] (death after a period of clinical deterioration in the signs and symptoms of heart failure despite medical treatment), arrhythmic events, and heart failure. SCD was defined as an unexpected death either within 1 h of the onset of cardiac symptoms in the absence of progressive cardiac deterioration; during sleep; or within 24 h of last being seen alive[6]. VF was defined as irregular or regular tachycardia with regards to polarity, amplitude, morphology, and sequence of intracardiac electrograms, with a mean cycle length of £240 ms (*i.e.*, ^{3}250 beats/min). Sustained VT was defined as tachycardia originating in the ventricle with a rate >100 beats/min and lasting > 30 s or requiring an intervention for termination. Appropriate ICD intervention was defined as a device shock or antitachycardia overdrive pacing delivered in response to a ventricular tachyarrhythmia and documented by stored intracardiac electrocardiogram data[7].

Data extraction and quality assessment

Data were extracted and analyzed by two independent investigators and were reported on standardized forms; consensus was reached through a discussion in case of disagreements. Moreover, data on hazard ratios (HRs) and 95% confidence intervals (CIs), adjusted and unadjusted variables in the regression model, author names, year of publication, sample size, age, percentage of male patients, LGE status (its presence, extent, location, and pattern), follow-up duration, LVEF, and left ventricular end-diastolic volume index (LVEDVi) were recorded if available.

The Newcastle–Ottawa Quality Assessment Scale (NOS) was used for quality assessment, as shown in Table 1, and the quality of the selected studies was evaluated and determined based on the selection of the study groups and the outcomes of interest. The NOS scoring system is as follows. A study scored 1 star for each item within the selection and outcome categories, and a maximum of 2 stars was given for comparability. Nine NOS stars were used to assess the risk of bias. A study with nine stars (four for selection, two for comparability, and three for outcome) was considered to have a low risk of bias, and a study with ≥ 5 stars (two for selection, one for comparability, and two for outcome) was considered to have a medium risk of bias. A study with < 5 stars (0 stars for either of the three fields or 1 star for comparability or outcome) was considered to have a high risk of bias.

Data analysis

Pooled HR and 95%CIs were calculated using a fixed-effects model. The heterogeneity between studies was assessed using Q and I^2 tests; heterogeneity was considered significant if I^2 ≥ 50%, and the studies will be recalculated using a random-effects model. Furthermore, the meta-analysis was performed using the D–L method if heterogeneity existed, and sensitivity analysis was used to assess the stability of the results.

Publication bias was evaluated using Egger's and Begg's tests; trim and fill analysis was used if there was publication bias. Sensitivity analysis using the leave-one-out method was performed, which allowed the calculation of estimates by omitting one study at a time. All analyses were performed using STATA, version 16. *P* values of < 0.05 were used to denote statistical significance.

The study has been registered with PROSPERO (number: CRD42023382021).

RESULTS

Search results

Figure 1 shows a flow chart for the search process and study selection. Overall, 147 citations were identified using PubMed (117 citations), Ovid MEDLINE (12 citations), and the Cochrane Library (18 citations). After screening the article titles and abstracts, 26 full-text articles of possible relevance were recruited, and 121 duplicate or irrelevant articles were excluded. Finally, 19 of the 26 relevant articles were included based on the inclusion criteria.

Quality assessment of the included studies

The quality of the included studies was assessed using the NOS, as shown in Table 1. None of the included studies had a high risk of bias; however, two studies had a low risk of bias[7,8]. For the study selection, 14 studies had a low risk of bias [6-19], and 5 had a medium risk of bias[3,5,20-22]. In terms of comparability, 8 studies had a low risk of bias[7-9,12,13,15,16,19], 7 studies had a medium risk of bias [3,11,14,17,18,21], and 5 studies had a high risk of bias[5,6,10,20,22]. Regarding outcomes, 8 studies had a low risk of bias [3,5,6,7,8,10,14,18] and 11 studies had a medium risk of bias[9,11-13,15-17,19-21,22].

Study characteristics

This study analyzed data from 7330 individuals (age ranging from 33 to 76 years; 68% were men) from 19 full-text studies from Asia, Europe, and North America. Of the 7330 patients, 2856 (39.0%) had myocardial LGE, and the follow-up duration ranged from 1 to 132 mo.

Among the 19 selected studies, 4 studies were multicenter[12,16,21,22] and 3 studies were retrospective studies[9,21,22]. 14 studies reported the relationship between the presence of LGE and adverse outcomes[3,5,7,6-14,17,18,21,22], 4

Table 1 Risk of bias assessment in the meta-analysis

Ref.	Selection				Comparability	Outcome			Total score
	Exposed cohort	Nonexposed cohort	Ascertainment of exposure	Outcome of interest		Assessment of outcome	Length of follow-up	Adequacy of follow-up	
Halliday *et al* [6], 2019	1	1	1	1	0	1	1	1	7
Gulati *et al* [2], 2013	0	1	1	1	1	1	1	1	7
Behera *et al* [9], 2020	1	1	1	1	2	0	1	1	8
Tateishi *et al* [10], 2015	1	1	1	1	0	1	1	1	7
Lehrke *et al* [11], 2011	1	1	1	1	1	1	0	1	7
Perazzolo *et al*[7], 2014	1	1	1	1	2	1	1	1	9
Neilan *et al* [12], 2013	1	1	1	1	2	1	0	1	8
Yamada *et al* [13], 2014	1	1	1	1	2	0	1	1	8
Buss *et al* [14], 2015	1	1	1	1	1	1	1	1	8
Mikami *et al* [15], 2016	1	1	1	1	2	1	0	1	8
Puntmann *et al*[16], 2016	1	1	1	1	2	1	0	1	8
Masci *et al* [17], 2012	1	1	1	1	1	1	0	1	7
Šramko *et al* [8], 2013	1	1	1	1	2	1	1	1	9
Amzulescu *et al*[20], 2015	0	1	1	1	0	0	1	1	5
Alba *et al* [21], 2020	1	1	1	0	1	0	1	1	6
Xu *et al*[18], 2021	1	1	1	1	1	1	1	1	8
Barison *et al* [19], 2020	1	1	1	1	2	0	1	1	8
Halliday *et al* [4], 2017	0	1	1	1	0	1	1	1	6
Di Marco *et al* [22], 2021	1	1	1	0	0	0	1	1	5

The total score was 9, and the higher the score, the lower the bias, besides, scores ≤ 5 means a relative high risk of bias.

studies that reported on the extent of LGE[3,12,16,20], 2 studies[6,15] that reported on the location of LGE and 1 study[6] that reported on the pattern of LGE were adjusted for age, sex, and LVEF, and a portion of those studies were modified for the New York Heart Association Functional Classification[5,6,10,11,21].

The detailed data on the author, year of publication, sample size, age, percentage of male patients, LGE status, follow-up duration, LVEF, and LVEDVi are shown in Table 2.

Data synthesis

Positivity for LGE and adverse outcomes: Overall, 18 studies, involving 7168 patients (2793 had LGE), reported the association between the positivity of LGE and adverse outcomes. The included outcomes of the subgroup analysis were all-cause mortality (4 articles), arrhythmic events (9 articles), and composite endpoints (12 articles). All-cause mortality

Table 2 Description of the studies included in the meta-analysis

Ref.	Type of study	Patients enrolled	Mean/median age (yr)	Male (%)	LGE present, *n* (%)	Mean/Median Follow-Up Time	Endpoint included in analysis	Mean/median LVEF (%)	Mean/median LVEDVi (mL/m²)
Halliday *et al*[6], 2019	Prospective	874	LGE negative: 51.0 ± 15.1; LGE extent (0.00%-2.55%): 52.8 ± 14.4; LGE extent (2.55%-5.10%): 53.7 ± 14.6; LGE extent (> 5.10%): 56.2 ± 14.6	588 (67.3)	300 (34.3)	4.9 yr (range, 3.5-7.0 yr)	All cause mortality; arrhythmic events: SCD and aborted SCD.	39 (range, 29-50)	LGE negative: 126.3 ± 36.6; the extent of LGE (0.00-2.55%): 147.9 ± 46.1; the extent of LGE (2.55%-5.10%): 142.8 ± 49.8; the extent of LGE (> 5.10%): 135.5 ± 37.3
Gulati *et al* [2], 2013	Prospective	472	51.1 ± 14.7	324 (68.6)	142 (30.1)	5.3 yr (range, 31 d-11.0 yr)	Arrhythmic events: SCD and aborted SCD; all cause mortality	37±13	135.1 ± 44.3
Behera *et al* [9], 2020	Retrospective	112	LGE negative: 45.5 (range, 33.0-58.7); LGE positive: 40.0 (range, 24.5-54.5)	LGE negative: 42 (61.8); LGE positive: 30 (68.2)	44 (39.3)	745 ± 320 d	Composite endpoint: All-cause mortality, resuscitated cardiac arrest, sustained VT/appropriate ICD shock, HF hospitalization	LGE negative: 31.5 (range, 28.0-36.2); LGE positive: 32.5 (range, 27.0-41.0)	LGE negative: 104.0 (range, 77.0-125.0); LGE positive: 137.0 (range, 87.5-225.2)
Tateishi *et al*[10], 2015	Prospective	207	50 ± 16	165 (80)	105 (50.7)	44 mo (range, 23-62 mo)	Composite endpoint: Cardiac death, cardiac transplantation, LV assist device implantation, appropriate ICD discharge for VT or VF, and rehospitalisation for HF	27 ± 11	143 ± 57
Lehrke *et al* [11], 2011	Prospective	184	51.55 ± 1.1	138 (75)	72 (39.1)	685 ± 30 d	Composite endpoint: Cardiac death, hospitalisation for decompensated HF, or appropriate ICD discharge	LGE negative: 44 (range, 33.1-50.9); LGE positive: 31 (range, 20.9-42.2)	LGE negative: 109 (range, 92.7-137.6); LGE positive: 133 (range, 116-161)
Perazzolo *et al*[7], 2014	Prospective	137	No arrhythmic events: 47 (range, 37-60); arrhythmic events: 59 (range, 43-70)	108 (78.8)	76 (55.5)	3 yr (range, 31 d-9.6 yr)	Arrhythmic events: SCD, cardiac arrest due to VF, sustained VT, or appropriate ICD intervention.	No arrhythmic events:33 (range, 28-40); arrhythmic events: 30 (range, 29-40)	No arrhythmic events: 109 (range, 87-140); arrhythmic events: 123 (range, 105-143)
Neilan *et al* [12], 2013	Prospective	162	55 ± 14	106 (65)	81 (50)	29 ± 18 mo	Composite endpoint: Cardiovascular death and appropriate ICD therapy; arrhythmic events: ATP, ICD discharge, and non-heart failure cardiovascular death	28 ± 9	140 ± 50
Yamada *et al*[13], 2014	Prospective	57	55 ± 13	40 (70.2)	25 (44)	71 ± 32 mo	Composite endpoint: Cardiac death, hospitalization for decompensated HF, or documented	LGE negative: 36 ± 13; LGE positive: 30 ± 11	LGE negative: 120 ± 39; LGE positive: 141 ± 47

							lethal arrhythmia, including VT and VF		
Buss *et al* [14], 2015	Prospective	210	52 ± 15	159 (76)	79 (38)	5.3 yr	Composite endpoint: Cardiac events together with the occurrence of hospitalization due to congestive HF	36.1 ± 13.8	132 ± 48
Mikami *et al*[15], 2016	Prospective	118	57 ± 14	68 (58)	66 (56)	2.1 ± 1.3 yr	Composite endpoint: Cardiac mortality or appropriate ICD therapy; arrhythmic events: Appropriate ICD therapy or SCD	32 ± 12	119 ± 42
Puntmann *et al*[16], 2016	Prospective	637	50 (range, 37-76 yr)	395 (62)	171 (27)	22 mo (range, 19-25 mo)	All cause mortality	47 (range, 29-50)	109 (range, 89-132)
Masci *et al* [17], 2012	Prospective	125	59 ± 14	82 (65.6)	50 (40)	14.2 mo (range, 6.5–28.8 mo)	Composite endpoint: Cardiac death and HF hospitalization	33 ± 10	LGE negative: 124 ± 35; LGE positive: 140 ± 39
Šramko *et al*[8], 2013	Prospective	42	Idiopathic: 45 ± 12; inflammatory: 42 ± 8	30 (71.4)	28 (66.7)	25 ± 9 mo	Composite endpoint: Cardiac death, urgent heart transplantation, and hospitalization for worsening HF	Idiopathic DC: 22 ± 11; Inflammatory DC: 21 ± 9	Idiopathic: 137 ± 39; Inflammatory: 148 ± 46
Amzulescu *et al*[20], 2015	Prospective	162	55 ± 15	102 (63.0)	63 (39)	3.4 yr (range, 1.5-6.3 yr)	Composite endpoint: Cardiovascular death, heart transplantation, LV assist device implantation, resuscitated cardiac arrest, and appropriate device shocks	24.6 ± 8.4	161.6 ± 52
Alba *et al* [21], 2020	Retrospective	1672	56 ± 14	1185 (70.9)	650 (39)	2.3 yr (range, 1.0-4.3 yr)	Composite endpoint: All-cause mortality, heart transplantation, or left ventricular assist device implant; arrhythmic events: SCD or appropriate ICD shock	33 ± 11	118 ± 27
Xu *et al* [18], 2021	Prospective	412	48.0 ± 14.4	300 (72.8)	201 (48.8)	28.1 mo (range, 19.3-43.0 mo)	Composite endpoint: All-cause mortality and HF readmission; all-cause mortality	23.7 ± 9.8	185.6 ± 58.9
Barison *et al*[19], 2020	Prospective	183	66 (range, 56-73 yr)	134 (73)	116 (63)	30 mo (range, 10-65 mo)	Composite endpoint: Appropriate ICD shock and cardiac death; arrhythmic events: appropriate ICD shock	24 (range, 21-31)	143 (range, 120-168)

Halliday *et al*[4], 2017	Prospective	399	49.9 ± 15.3	254 (63.7)	101 (25.3)	4.6 yr (range, 3.5-7.0 yr)	Arrhythmic events: SCD or Aborted SCD	49.6 ± 4.9	111.1 ± 19.4
Di Marco *et al*[22], 2021	Retrospective	1165	58 (range, 48-68)	768 (65.9)	486 (41.7)	36 mo (range, 20-58 mo)	Arrhythmic events: Appropriate ICD therapies, sustained VT, resuscitated cardiac arrest, and sudden death	39 (range, 30-46)	118 (range, 99-142)

Values are *n*, mean ± SD, or *n* (%) unless otherwise indicated; LGE: Late gadolinium enhancement; VT: Ventricular tachycardia; VF: Ventricular fibrillation; HF: Heart failure; ICD: Implantable cardioverter-defibrillator; SCD: Sudden cardiac death; LV: Left ventricular; ATP: Anti-tachycardia pacing.

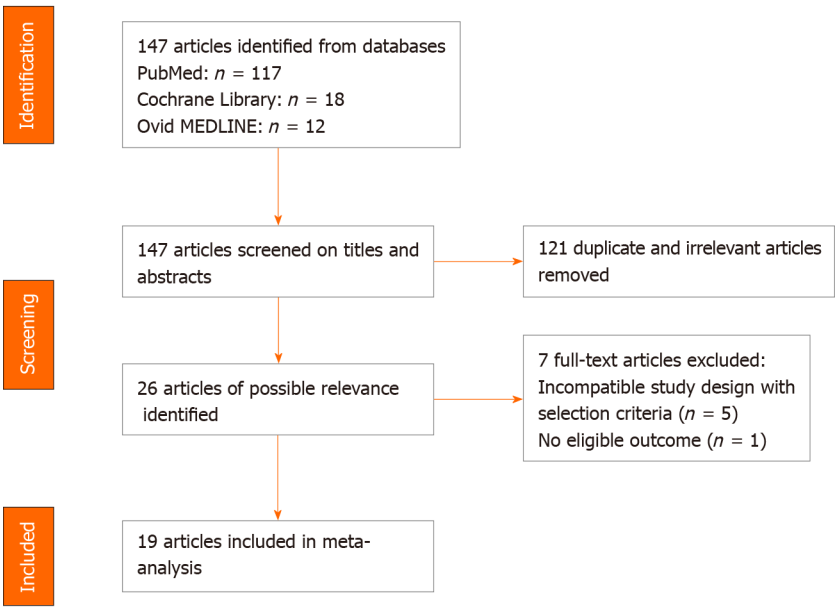

DOI: 10.4329/wjr.v15.i11.324

Figure 1 Flow diagram of the selection of articles.

occurred in 313 patients (4.4% of patients of the 18 included studies), of who 172 had LGE (6.2% of LGE-positive patients) and 141 had no LGE (3.2% of LGE-negative patients), with a risk difference between LGE-positive and LGE-negative patients of 12.2% (95%CI: 9.1%–15.3%; $P < 0.001$). Besides, arrhythmic events and composite endpoints occurred in 256 (3.6%) and 603 (8.4%) patients, respectively.

In the pooled analysis, positivity for LGE was associated with an increased risk of all-cause mortality (HR: 2.14; 95%CI: 1.68–2.72; $P < 0.001$), arrhythmic events (HR: 5.12, 95%CI: 3.24–8.07, $P < 0.001$), and composite endpoints (HR: 2.38, 95%CI: 1.83–3.11, $P < 0.001$), as shown in Figure 2. A random-effects model was used for studies on arrhythmic events with significant heterogeneity ($I^2 = 67.9\%$; $P = 0.002$), and sensitivity analysis using the leave-one-out method showed that the study by Alba *et al*[21] may be the source of heterogeneity. However, Egger's and Begg's tests showed that there was publication bias in the presence of LGE and composite endpoints; after conducting a trim and fill analysis and adjusting for the effect size for funnel plot asymmetry, the *P* values before and after the trim and fill analysis were less than 0.001, indicating that no significant changes occurred and the results were reliable.

The extent of LGE and adverse outcomes: Two studies were included in the subgroup analysis of all-cause mortality, including 313 participants with LGE and 796 without LGE, with 101 all-cause mortality occurred during the follow-up period, and the pooled HR of all-cause mortality for every 1% increment in the extent of LGE was 1.10 (95%CI: 1.06–1.14; $P < 0.001$) (Figure 3A). In the analysis of the outcome of composite endpoints, two studies recruited 179 patients with LGE and 166 without LGE, with 79 composite endpoints occurred during the follow-up period, however, even random-effects model was used for studies on composite endpoints with significant heterogeneity ($I^2 = 64.0\%$; $P = 0.096$); the result showed that every 1% increment in the extent of LGE only has numerically increased the risk of composite endpoints without reaching statistical significance 1.22 (95%CI: 0.91–1.63; $P < 0.001$).

The LGE locations and adverse outcomes: Recently, several LGE metrics, including location and pattern, have emerged as new indicators for risk prediction. Subgroup analysis, which included two studies (LGE was present in 501 patients and absent in 785 patients; all-cause mortality occurred in 212 patients), showed that LGE located in the septum (pooled

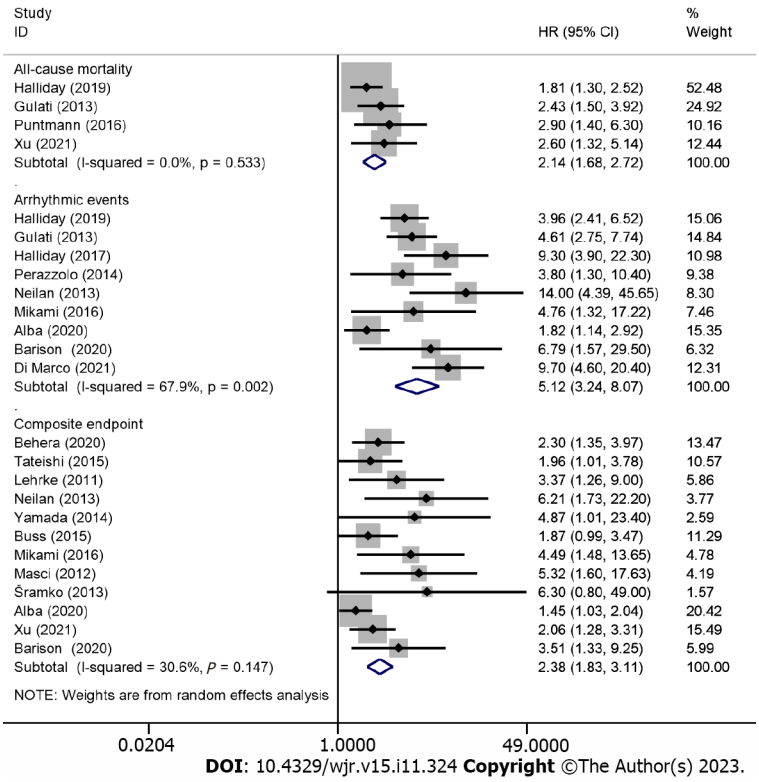

Figure 2 The forest plot of risk of adverse outcomes in dilated cardiomyopathy patients with the presence of late gadolinium enhancement.

HR: 1.64; 95%CI: 1.20–2.22; $P < 0.001$) and in both the septum and free wall (pooled HR: 1.68; 95%CI: 1.39–2.02; $P < 0.001$) can predict all-cause mortality. However, LGE located in the free wall only has numerically increased the risk of all-cause mortality without reaching statistical significance (pooled HR: 2.07; 95%CI: 0.31–13.98; $P = 0.457$) (Figure 3B). A random-effects model was used for studies on free-wall LGE with significant heterogeneity ($I^2 = 87.1\%$; $P = 0.005$).

The subgroup analysis for predicting composite endpoints included five studies (Figure 3C), including 471 LGE-positive participants and 466 LGE-negative participants, and the number of composite endpoints was 297. The pooled HRs for septal and inferior LGE of composite endpoints were 2.40 (95%CI: 1.12–5.14, $P = 0.025$) and 2.95 (95%CI: 1.81–4.81, $P < 0.001$), respectively; a random-effects model was used to analyze the heterogeneity in the septal LGE group ($I^2 = 84.1\%$; $P = 0.002$), sensitivity analysis using the leave-one-out method showed that the study by Xu *et al*[18]. may be the source of heterogeneity, and the heterogeneity may result from the unadjusted HR.

The LGE patterns and adverse outcomes: In addition to the mid-wall pattern of LGE, recent studies have found that LGE has many other patterns, such as focal and sub-epicardial patterns, which can also provide stratification information for adverse outcomes. Subgroup analysis for all-cause mortality, which included 501 patients with myocardial LGE and 785 without LGE from two studies, was performed for the mid-wall, focal, and multiple (mid-wall, sub-epicardial, and focal) patterns of LGE; death occurred in 212 patients, and the pooled HRs were 1.81 (95%CI: 1.31–2.52; $P < 0.001$), 1.23 (95%CI: 0.11–13.40; $P = 0.867$; not statistical significance), and 1.53 (95%CI: 1.12–2.10; $P < 0.001$), respectively (Figure 3D).

The relationship between the patterns of LGE and composite endpoints was also analyzed; subgroup analysis was performed and included two studies involving 245 LGE-positive patients and 279 LGE-negative patients, with 195 composite endpoints during the follow-up period. Our analysis showed that mid-wall (pooled HR: 2.13; 95%CI: 1.39–3.27; $P = 0.001$) patterns of LGE can predict composite endpoints (Figure 3E), even random-effects model was used for studies on sub-epicardial LGE with significant heterogeneity ($I^2 = 65.0\%$; $P = 0.091$), these results showed that sub-epicardial LGE has numerically increased the risk of composite endpoints without reaching statistical significance (pooled HR: 1.81; 95%CI: 0.73–4.51; $P = 0.202$).

Positive effect of LGE and arrhythmic events on different ranges of LVEF: As the studies included in our meta-analysis all demonstrated indications of LVEF, we also performed a subgroup analysis to assess the impact of LGE on DCM for different ranges of LVEF by dividing those studies into two groups (LVEF < 35% and LVEF ≥ 35%). The analysis, which included nine studies (LGE was present in 2018 patients and absent in 3164 patients; arrhythmic events occurred in 256 patients), showed that LGE is a stronger predictor of arrhythmic events in patients with a greater LVEF, and the pooled HRs for positive LGE with LVEF < 35% and LVEF ≥ 35% were 4.49 (95%CI: 2.00–10.10; $P < 0.001$) and 5.79 (95%CI: 3.74–8.95; $P < 0.001$), respectively (Figure 3F). A random-effects model was used for studies on LVEF < 35% with significant heterogeneity ($I^2 = 68.8\%$; $P = 0.012$).

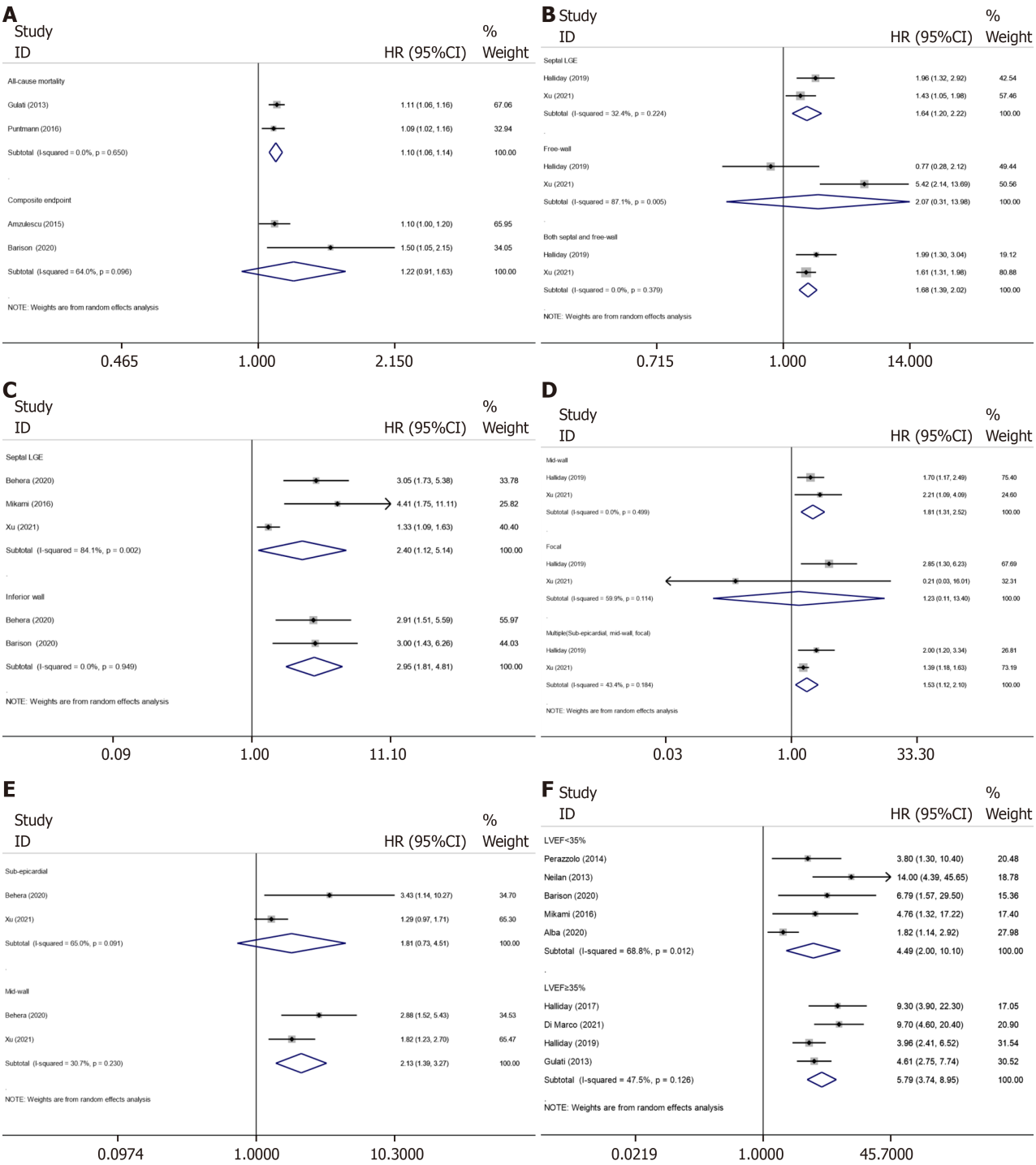

DOI: 10.4329/wjr.v15.i11.324

Figure 3 The forest plot of association between extent, location, and pattern of late gadolinium enhancement and adverse outcomes. A: Association between extent of late gadolinium enhancement (LGE) and adverse outcomes; B: Association between locations of LGE and all-cause mortality; C: Association between locations of LGE and composite endpoint; D: Association between patterns of LGE and all-cause mortality; E: Association between patterns of LGE and composite endpoint; F: Association between the positive of LGE and arrhythmic events in different ranges of left ventricular ejection fraction.

DISCUSSION

LGE detected by CMR represents a myocardial scar, which could provide a foundation for ventricular re-entrant arrhythmia and is the main cause of SCD in multiple myocardiopathies[23]. Although LGE is observed in approximately 30% of patients with DCM, several studies support the prognostic power of LGE[3,4]. This meta-analysis included 7330 patients with DCM, confirmed the prognostic value of LGE for multiple adverse endpoints, and investigated the association between the extent, location, and pattern of LGE and outcomes.

Prior meta-analyses have evaluated the prognostic value of LGE in DCM[24-26]. However, the sample size of our meta-analysis was larger, and given the increasing numbers of studies published in the past few years about the characteristics

of LGE (extent, location, and pattern), we considered that focusing on novel indicators was appropriate. The relevant number of studies included allowed subgroup analyses between the extent, location, and pattern of LGE and outcomes.

The presence of LGE and adverse outcomes

Myocardial fibrosis is strongly associated with ventricular remodeling[11,27]. The prognostic value of LGE is independent of left ventricular parameters and can provide additional information on LVEF[28]. Additionally, the predictive ability of LGE was found to be better in patients with higher LVEF[22].

In our meta-analysis, LGE was present in approximately 40% of the patients with DCM under study and was strongly and significantly associated with multiple adverse outcomes. The relationship between LGE and the endpoints was particularly obvious for arrhythmic events (pooled HR: 5.12, 95%CI: 3.24–8.07, $P < 0.001$). This will be extremely meaningful for risk stratification mainly based on LVEF, as most SCD cases did not have severely reduced LVEF[23]. Moreover, the finding that the predictive power of LGE was better in patients with greater LVEF regarding the endpoint of arrhythmic events in our subgroup analysis confirmed the results of a previous study[22]. The severely reduced LVEF detected in patients with DCM represents an adversely remodeled left ventricle, which can lead to self-organized criticality and cascading mechanical collapse, and ultimately result in SCD[29]. However, in the absence of a severely remodeled left ventricle, LGE provides the foundation for ventricular re-entrant arrhythmia, which can be the major cause of adverse outcomes.

The extent of LGE and adverse outcomes

A study suggests that the susceptibility to re-entrant arrhythmias may be increased with the extent of LGE[19], indicating that the evaluation of the extent of LGE plays an important role in determining the prognosis of patients with DCM.

As a continuous variable, every 1% increment in LGE extent can predict all-cause mortality in our meta-analysis. However, even though only studies that quantified the extent of LGE as a percentage of the left ventricular mass were included in our meta-analysis, heterogeneity among studies was inevitable because of the differences in the measurement methods and parameters of LGE quantification used among the included studies. However, Halliday *et al*[6] and Behera *et al*[9] demonstrated that the correlation between the extent of LGE and outcomes seems to be nonlinear, as a small increase in the extent of LGE could significantly increase the risk of adverse outcomes.

One potential mechanism is that the induction of arrhythmia can be influenced by the texture and spatial distribution of fibrosis, the formation and dynamics of which are mostly determined by the maximal local fibrosis level; thus, the composition of myocardial fibrosis, rather than volume, may be the main determinant of arrhythmia[30]. Another mechanism that may explain these results is that ventricular arrhythmia most likely originates from the regions between myocardial fibrosis and healthy tissue with slow conduction[31,32]. Therefore, more precise identification of heterogeneous zones between healthy myocardium and myocardial fibrosis and the accurate discrimination of the texture and type of myocardial fibrosis may help better predict the prognosis of patients with DCM.

The LGE locations and adverse outcomes

Studies mainly focused on septal LGE, which is the most common location of LGE. However, recent studies have shown that LGE can also occur in the free wall with a high incidence[6,18], suggesting that LGE located in this location is worth further exploration.

Our meta-analysis found that septal LGE is associated with all-cause mortality and composite endpoints, which is consistent with the findings of previous studies. Furthermore, combined septal and free-wall LGE was more closely associated with all-cause mortality, as multi-location LGE may result in a larger extent of myocardial fibrosis.

The location of LGE may be related to its underlying etiology. LGE of idiopathic DCM is frequently located in the septum for unclear reasons, whereas LGE of DCM caused by viral myocarditis is usually located in the free wall. This is because cardiotropic viruses that originate from the bloodstream can cause pericarditis; the free wall in direct contact with the pericardium is the prime location for migration of inflammatory cells. The scar microstructure may be varied for the underlying etiology and cause a different risk[33].

However, because the number of studies included in this study was small and whether free-wall LGE is a protective or adverse factor remains controversial[6,18], further investigation regarding the prognosis of the distribution of LGE is still required.

The LGE patterns and adverse outcomes

As the most typical LGE pattern, mid-wall LGE was associated with an increased risk of all-cause mortality and composite endpoints in this study. However, our subgroup analyses showed that sub-epicardial and focal pattern of LGE were not statistically significant in predicting adverse outcome; in this case, more studies are required to confirm their prognostic value.

The sub-endocardial and transmural patterns of LGE have been considered to be indicators of previous myocardial infarction[34,35]. However, several studies have investigated the role of transmural LGE, which is not coherent with coronary artery territory (indicating that this pattern is not of an ischemic origin), and sub-endocardial LGE in determining the prognosis of patients with DCM[21,22]. Di Marco *et al*[22] have found that transmural LGE was associated with a heightened risk of adverse outcomes. Through the aforementioned studies, it is suggested that more attention should be paid to those "ischemia LGE patterns" rather than simply seeing it as myocardial infarct in patients with DCM.

In addition to focusing on the pattern of LGE itself, the number of coexisting LGE patterns must also be considered. In our meta-analysis, patients with multiple patterns of LGE (sub-epicardial, mid-wall, and focal) were at a greater risk of

all-cause mortality than those without LGE. One possibility is that more LGE patterns may represent a higher heterogeneity of fibrosis. However, the prognostic ability of multiple LGE patterns is not as good as that of one single pattern in some other studies[6,18]. The limited number of patients with multiple LGE patterns may be responsible for the controversial results. Therefore, more trials are needed to draw a more certain conclusion.

Furthermore, Di Marco *et al*[22] have found that the combination of LVEF strata and LGE status may help improve risk stratification in patients with DCM. Based on the results of this study, the next subdivision of various indicators (extent, location, and pattern) of LGE, particularly the free-wall LGE, and the integration of those indicators with varying clinical parameters may be more helpful in predicting the prognosis of patients with DCM.

Study limitations

The limitations of this study are that most included studies were observational; selection bias should be anticipated; and this meta-analysis can only detect associations but not causality. Additionally, the exclusion and inclusion criteria were different among the included studies, and there was a wide variety on the definitions of the endpoints. Finally, the data on the location and pattern of LGE were limited, which can explain the significant heterogeneity in some subgroup analyses; further studies enrolling more eligible patients are required.

CONCLUSION

CMR-LGE exhibited a substantial prognostic value in predicting all-cause mortality, arrhythmic events and composite endpoints in patients with DCM. The extent, location, and pattern of LGE could provide additional information for risk stratification.

ARTICLE HIGHLIGHTS

Research background

LGE as a prognostic indicator of dilated cardiomyopathy (DCM) has been extensively studied, and several new metrics of late gadolinium enhancement (LGE), such as its extent, location, and pattern, have emerged. However, whether some indicators are protective or risk factors and whether the combination of left ventricular ejection fraction (LVEF) strata and LGE has a better predictive value remains controversial; therefore, further discussion is required, and more precise risk stratification should be explored.

Research motivation

This meta-analysis aimed to detect the predictive performance of the extent, location, and pattern of LGE, to compare and screen these new indicators of LGE, and provide novel concepts for improving the risk stratification algorithm for adverse outcomes of DCM.

Research objectives

The research objectives of this meta-analysis were to investigate the associations between the positivity and extent, location, and pattern of LGE derived from CMR and multiple outcomes. We found that the presence of LGE was associated with an increased risk of multiple adverse outcomes (all-cause mortality, arrhythmic events, and composite endpoints). Furthermore, an increase in the extent of LGE and a different location and pattern of LGE may impact the prognosis. Although the current studies and meta-analyses mainly focus on the relationship between the presence of LGE and prognosis, our study found that LGE is a stronger predictor of arrhythmic events in patients with greater LVEF, and that the different types of LGE were equally predictive, which suggested that these new indicators and their combinations may help improve the risk stratification.

Research methods

We followed the guidelines of PRISMA-NMA, registered with PROSPERO, and extracted data from databases recommended by the Cochrane Handbook. After discussion, we reached a consensus and classified the endpoints into three; the pooled HRs and 95%CIs obtained by using STATA were applied to evaluate the effectiveness of the new metrics of LGE. The Newcastle–Ottawa Quality Assessment Scale was used for quality assessment. Publication bias was assessed using Egger's and Begg's tests, and a sensitivity analysis was performed using the leave-one-out method, to assess the stability of the results.

Research results

CMR-LGE is a strong prognostic marker for patients with DCM. The extent, location, and pattern of LGE provided additional information for risk stratification. Further studies are needed to determine whether free-wall LGE is a protective or risk factor, and whether the focal or sub-epicardial pattern of LGE has predictive value.

Research conclusions

CMR-LGE is a strong prognostic marker for patients with DCM. The extent, location, and pattern of LGE provided

additional information for risk stratification. Further studies are needed to determine whether free-wall LGE is a protective or risk factor, and whether the focal or sub-epicardial pattern of LGE has predictive value.

Research perspectives

The prognostic value of different locations and patterns of LGE needs to be confirmed in future studies, and the combined predictive value of these predictors warrants further exploration.

FOOTNOTES

Co-first authors: Xin-Yi Feng and Wen-Feng He.

Author contributions: Feng XY participated in the study design, contributed to data analysis and interpretation, and drafted the manuscript; He WF contributed to the preparation, editing and review of the manuscript; Zhang TY carried out data acquisition, performed data analysis and interpretation and edited the manuscript; Wang LL, Feng YL, and Li CP carried out data acquisition and performed data analysis and interpretation; Li R contributed to quality control of data and algorithm, and editing and review of the manuscript; All authors read and approved the final manuscript.

Supported by the Research Grant of the National Natural Science Foundation of China, No. 81801674; Sichuan Province Science and Technology Support Program, No. 2021YJ0242.

Conflict-of-interest statement: All the authors declare that they have no competing interests.

PRISMA 2009 Checklist statement: The authors have read the PRISMA 2009 Checklist, and the manuscript was prepared and revised according to the PRISMA 2009 Checklist.

Country/Territory of origin: China

ORCID number: Rui Li 0000-0002-5716-9259.

S-Editor: Liu JH
L-Editor: A
P-Editor: Liu JH

REFERENCES

1 **Jefferies JL**, Towbin JA. Dilated cardiomyopathy. *Lancet* 2010; **375**: 752-762 [PMID: 20189027 DOI: 10.1016/S0140-6736(09)62023-7]

2 **Gulati A**, Jabbour A, Ismail TF, Guha K, Khwaja J, Raza S, Morarji K, Brown TD, Ismail NA, Dweck MR, Di Pietro E, Roughton M, Wage R, Daryani Y, O'Hanlon R, Sheppard MN, Alpendurada F, Lyon AR, Cook SA, Cowie MR, Assomull RG, Pennell DJ, Prasad SK. Association of fibrosis with mortality and sudden cardiac death in patients with nonischemic dilated cardiomyopathy. *JAMA* 2013; **309**: 896-908 [PMID: 23462786 DOI: 10.1001/jama.2013.1363]

3 **Leyva F**, Taylor RJ, Foley PW, Umar F, Mulligan LJ, Patel K, Stegemann B, Haddad T, Smith RE, Prasad SK. Left ventricular midwall fibrosis as a predictor of mortality and morbidity after cardiac resynchronization therapy in patients with nonischemic cardiomyopathy. *J Am Coll Cardiol* 2012; **60**: 1659-1667 [PMID: 23021326 DOI: 10.1016/j.jacc.2012.05.054]

4 **Halliday BP**, Gulati A, Ali A, Guha K, Newsome S, Arzanauskaite M, Vassiliou VS, Lota A, Izgi C, Tayal U, Khalique Z, Stirrat C, Auger D, Pareek N, Ismail TF, Rosen SD, Vazir A, Alpendurada F, Gregson J, Frenneaux MP, Cowie MR, Cleland JGF, Cook SA, Pennell DJ, Prasad SK. Association Between Midwall Late Gadolinium Enhancement and Sudden Cardiac Death in Patients With Dilated Cardiomyopathy and Mild and Moderate Left Ventricular Systolic Dysfunction. *Circulation* 2017; **135**: 2106-2115 [PMID: 28351901 DOI: 10.1161/CIRCULATIONAHA.116.026910]

5 **Hutton B**, Salanti G, Caldwell DM, Chaimani A, Schmid CH, Cameron C, Ioannidis JP, Straus S, Thorlund K, Jansen JP, Mulrow C, Catalá-López F, Gøtzsche PC, Dickersin K, Boutron I, Altman DG, Moher D. The PRISMA extension statement for reporting of systematic reviews incorporating network meta-analyses of health care interventions: checklist and explanations. *Ann Intern Med* 2015; **162**: 777-784 [PMID: 26030634 DOI: 10.7326/M14-2385]

6 **Halliday BP**, Baksi AJ, Gulati A, Ali A, Newsome S, Izgi C, Arzanauskaite M, Lota A, Tayal U, Vassiliou VS, Gregson J, Alpendurada F, Frenneaux MP, Cook SA, Cleland JGF, Pennell DJ, Prasad SK. Outcome in Dilated Cardiomyopathy Related to the Extent, Location, and Pattern of Late Gadolinium Enhancement. *JACC Cardiovasc Imaging* 2019; **12**: 1645-1655 [PMID: 30219397 DOI: 10.1016/j.jcmg.2018.07.015]

7 **Perazzolo Marra M**, De Lazzari M, Zorzi A, Migliore F, Zilio F, Calore C, Vettor G, Tona F, Tarantini G, Cacciavillani L, Corbetti F, Giorgi B, Miotto D, Thiene G, Basso C, Iliceto S, Corrado D. Impact of the presence and amount of myocardial fibrosis by cardiac magnetic resonance on arrhythmic outcome and sudden cardiac death in nonischemic dilated cardiomyopathy. *Heart Rhythm* 2014; **11**: 856-863 [PMID: 24440822 DOI: 10.1016/j.hrthm.2014.01.014]

8 **Šramko M**, Kubánek M, Tintěra J, Kautznerová D, Weichet J, Malušková J, Franeková J, Kautzner J. Utility of combination of cardiac magnetic resonance imaging and high-sensitivity cardiac troponin T assay in diagnosis of inflammatory cardiomyopathy. *Am J Cardiol* 2013; **111**: 258-264 [PMID: 23102878 DOI: 10.1016/j.amjcard.2012.09.024]

9 **Behera DR**, V K AK, K K NN, S S, Nair KKM, G S, T R K, Gopalakrishnan A, S H. Prognostic value of late gadolinium enhancement in cardiac MRI of non-ischemic dilated cardiomyopathy patients. *Indian Heart J* 2020; **72**: 362-368 [PMID: 33189195 DOI: 10.1016/j.ihj.2020.06.011]

10 **Tateishi E**, Noguchi T, Goto Y, Morita Y, Ishibashi-Ueda H, Yamada N, Kanzaki H, Nishimura K, Miyamoto Y, Anzai T, Ogawa H, Yasuda S. Prognostic impact of blood pressure response plus gadolinium enhancement in dilated cardiomyopathy. *Heart* 2015; **101**: 774-780 [PMID: 25761994 DOI: 10.1136/heartjnl-2014-307007]

11 **Lehrke S**, Lossnitzer D, Schöb M, Steen H, Merten C, Kemmling H, Pribe R, Ehlermann P, Zugck C, Korosoglou G, Giannitsis E, Katus HA. Use of cardiovascular magnetic resonance for risk stratification in chronic heart failure: prognostic value of late gadolinium enhancement in patients with non-ischaemic dilated cardiomyopathy. *Heart* 2011; **97**: 727-732 [PMID: 21097819 DOI: 10.1136/hrt.2010.205542]

12 **Neilan TG**, Coelho-Filho OR, Danik SB, Shah RV, Dodson JA, Verdini DJ, Tokuda M, Daly CA, Tedrow UB, Stevenson WG, Jerosch-Herold M, Ghoshhajra BB, Kwong RY. CMR quantification of myocardial scar provides additive prognostic information in nonischemic cardiomyopathy. *JACC Cardiovasc Imaging* 2013; **6**: 944-954 [PMID: 23932642 DOI: 10.1016/j.jcmg.2013.05.013]

13 **Yamada T**, Hirashiki A, Okumura T, Adachi S, Shimazu S, Shimizu S, Morimoto R, Takeshita K, Naganawa S, Kondo T, Murohara T. Prognostic impact of combined late gadolinium enhancement on cardiovascular magnetic resonance and peak oxygen consumption in ambulatory patients with nonischemic dilated cardiomyopathy. *J Card Fail* 2014; **20**: 825-832 [PMID: 25151210 DOI: 10.1016/j.cardfail.2014.08.005]

14 **Buss SJ**, Breuninger K, Lehrke S, Voss A, Galuschky C, Lossnitzer D, Andre F, Ehlermann P, Franke J, Taeger T, Frankenstein L, Steen H, Meder B, Giannitsis E, Katus HA, Korosoglou G. Assessment of myocardial deformation with cardiac magnetic resonance strain imaging improves risk stratification in patients with dilated cardiomyopathy. *Eur Heart J Cardiovasc Imaging* 2015; **16**: 307-315 [PMID: 25246506 DOI: 10.1093/ehjci/jeu181]

15 **Mikami Y**, Cornhill A, Heydari B, Joncas SX, Almehmadi F, Zahrani M, Bokhari M, Stirrat J, Yee R, Merchant N, Lydell CP, Howarth AG, White JA. Objective criteria for septal fibrosis in non-ischemic dilated cardiomyopathy: validation for the prediction of future cardiovascular events. *J Cardiovasc Magn Reson* 2016; **18**: 82 [PMID: 27839514 DOI: 10.1186/s12968-016-0300-z]

16 **Puntmann VO**, Carr-White G, Jabbour A, Yu CY, Gebker R, Kelle S, Hinojar R, Doltra A, Varma N, Child N, Rogers T, Suna G, Arroyo Ucar E, Goodman B, Khan S, Dabir D, Herrmann E, Zeiher AM, Nagel E; International T1 Multicentre CMR Outcome Study. T1-Mapping and Outcome in Nonischemic Cardiomyopathy: All-Cause Mortality and Heart Failure. *JACC Cardiovasc Imaging* 2016; **9**: 40-50 [PMID: 26762873 DOI: 10.1016/j.jcmg.2015.12.001]

17 **Masci PG**, Barison A, Aquaro GD, Pingitore A, Mariotti R, Balbarini A, Passino C, Lombardi M, Emdin M. Myocardial delayed enhancement in paucisymptomatic nonischemic dilated cardiomyopathy. *Int J Cardiol* 2012; **157**: 43-47 [PMID: 21176853 DOI: 10.1016/j.ijcard.2010.11.005]

18 **Xu Y**, Lin J, Liang Y, Wan K, Li W, Wang J, Zhu Y, Mui D, Wang L, Li Y, Cheng W, Sun J, Zhang Q, Han Y, Chen Y. Prognostic value of left ventricular remodelling index in idiopathic dilated cardiomyopathy. *Eur Heart J Cardiovasc Imaging* 2021; **22**: 1197-1207 [PMID: 32658979 DOI: 10.1093/ehjci/jeaa144]

19 **Barison A**, Aimo A, Mirizzi G, Castiglione V, Ripoli A, Panchetti L, Rossi A, Giannoni A, Startari U, Aquaro GD, Emdin M, Piacenti M. The extent and location of late gadolinium enhancement predict defibrillator shock and cardiac mortality in patients with non-ischaemic dilated cardiomyopathy. *Int J Cardiol* 2020; **307**: 180-186 [PMID: 32067833 DOI: 10.1016/j.ijcard.2020.02.028]

20 **Amzulescu MS**, Rousseau MF, Ahn SA, Boileau L, de Meester de Ravenstein C, Vancraeynest D, Pasquet A, Vanoverschelde JL, Pouleur AC, Gerber BL. Prognostic Impact of Hypertrabeculation and Noncompaction Phenotype in Dilated Cardiomyopathy: A CMR Study. *JACC Cardiovasc Imaging* 2015; **8**: 934-946 [PMID: 26189121 DOI: 10.1016/j.jcmg.2015.04.015]

21 **Alba AC**, Gaztañaga J, Foroutan F, Thavendiranathan P, Merlo M, Alonso-Rodriguez D, Vallejo-García V, Vidal-Perez R, Corros-Vicente C, Barreiro-Pérez M, Pazos-López P, Perez-David E, Dykstra S, Flewitt J, Pérez-Rivera JÁ, Vazquez-Caamaño M, Katz SD, Sinagra G, Køber L, Poole J, Ross H, Farkouh ME, White JA. Prognostic Value of Late Gadolinium Enhancement for the Prediction of Cardiovascular Outcomes in Dilated Cardiomyopathy: An International, Multi-Institutional Study of the MINICOR Group. *Circ Cardiovasc Imaging* 2020; **13**: e010105 [PMID: 32312112 DOI: 10.1161/CIRCIMAGING.119.010105]

22 **Di Marco A**, Brown PF, Bradley J, Nucifora G, Claver E, de Frutos F, Dallaglio PD, Comin-Colet J, Anguera I, Miller CA, Schmitt M. Improved Risk Stratification for Ventricular Arrhythmias and Sudden Death in Patients With Nonischemic Dilated Cardiomyopathy. *J Am Coll Cardiol* 2021; **77**: 2890-2905 [PMID: 34112317 DOI: 10.1016/j.jacc.2021.04.030]

23 **Stecker EC**, Vickers C, Waltz J, Socoteanu C, John BT, Mariani R, McAnulty JH, Gunson K, Jui J, Chugh SS. Population-based analysis of sudden cardiac death with and without left ventricular systolic dysfunction: two-year findings from the Oregon Sudden Unexpected Death Study. *J Am Coll Cardiol* 2006; **47**: 1161-1166 [PMID: 16545646 DOI: 10.1016/j.jacc.2005.11.045]

24 **Becker MAJ**, Cornel JH, van de Ven PM, van Rossum AC, Allaart CP, Germans T. The Prognostic Value of Late Gadolinium-Enhanced Cardiac Magnetic Resonance Imaging in Nonischemic Dilated Cardiomyopathy: A Review and Meta-Analysis. *JACC Cardiovasc Imaging* 2018; **11**: 1274-1284 [PMID: 29680351 DOI: 10.1016/j.jcmg.2018.03.006]

25 **Di Marco A**, Anguera I, Schmitt M, Klem I, Neilan TG, White JA, Sramko M, Masci PG, Barison A, Mckenna P, Mordi I, Haugaa KH, Leyva F, Rodriguez Capitán J, Satoh H, Nabeta T, Dallaglio PD, Campbell NG, Sabaté X, Cequier Á. Late Gadolinium Enhancement and the Risk for Ventricular Arrhythmias or Sudden Death in Dilated Cardiomyopathy: Systematic Review and Meta-Analysis. *JACC Heart Fail* 2017; **5**: 28-38 [PMID: 28017348 DOI: 10.1016/j.jchf.2016.09.017]

26 **Duan X**, Li J, Zhang Q, Zeng Z, Luo Y, Jiang J, Chen Y. Prognostic value of late gadolinium enhancement in dilated cardiomyopathy patients: a meta-analysis. *Clin Radiol* 2015; **70**: 999-1008 [PMID: 26116301 DOI: 10.1016/j.crad.2015.05.007]

27 **Wu KC**, Weiss RG, Thiemann DR, Kitagawa K, Schmidt A, Dalal D, Lai S, Bluemke DA, Gerstenblith G, Marbán E, Tomaselli GF, Lima JA. Late gadolinium enhancement by cardiovascular magnetic resonance heralds an adverse prognosis in nonischemic cardiomyopathy. *J Am Coll Cardiol* 2008; **51**: 2414-2421 [PMID: 18565399 DOI: 10.1016/j.jacc.2008.03.018]

28 **Assomull RG**, Prasad SK, Lyne J, Smith G, Burman ED, Khan M, Sheppard MN, Poole-Wilson PA, Pennell DJ. Cardiovascular magnetic resonance, fibrosis, and prognosis in dilated cardiomyopathy. *J Am Coll Cardiol* 2006; **48**: 1977-1985 [PMID: 17112987 DOI: 10.1016/j.jacc.2006.07.049]

29 **Packer M**. What causes sudden death in patients with chronic heart failure and a reduced ejection fraction? *Eur Heart J* 2020; **41**: 1757-1763

[PMID: 31390006 DOI: 10.1093/eurheartj/ehz553]

30 **Kazbanov IV**, ten Tusscher KH, Panfilov AV. Effects of Heterogeneous Diffuse Fibrosis on Arrhythmia Dynamics and Mechanism. *Sci Rep* 2016; **6**: 20835 [PMID: 26861111 DOI: 10.1038/srep20835]

31 **Hsia HH**, Marchlinski FE. Electrophysiology studies in patients with dilated cardiomyopathies. *Card Electrophysiol Rev* 2002; **6**: 472-481 [PMID: 12438831 DOI: 10.1023/a:1021109130276]

32 **Estner HL**, Zviman MM, Herzka D, Miller F, Castro V, Nazarian S, Ashikaga H, Dori Y, Berger RD, Calkins H, Lardo AC, Halperin HR. The critical isthmus sites of ischemic ventricular tachycardia are in zones of tissue heterogeneity, visualized by magnetic resonance imaging. *Heart Rhythm* 2011; **8**: 1942-1949 [PMID: 21798226 DOI: 10.1016/j.hrthm.2011.07.027]

33 **Mahrholdt H**, Wagner A, Deluigi CC, Kispert E, Hager S, Meinhardt G, Vogelsberg H, Fritz P, Dippon J, Bock CT, Klingel K, Kandolf R, Sechtem U. Presentation, patterns of myocardial damage, and clinical course of viral myocarditis. *Circulation* 2006; **114**: 1581-1590 [PMID: 17015795 DOI: 10.1161/CIRCULATIONAHA.105.606509]

34 **McCrohon JA**, Moon JC, Prasad SK, McKenna WJ, Lorenz CH, Coats AJ, Pennell DJ. Differentiation of heart failure related to dilated cardiomyopathy and coronary artery disease using gadolinium-enhanced cardiovascular magnetic resonance. *Circulation* 2003; **108**: 54-59 [PMID: 12821550 DOI: 10.1161/01.CIR.0000078641.19365.4C]

35 **Zhao S**. Letter to the editor: is it time for imaging to level with pathology? *Int J Cardiovasc Imaging* 2020; **36**: 2249-2250 [PMID: 32677022 DOI: 10.1007/s10554-020-01936-z]

Published by **Baishideng Publishing Group Inc**
7041 Koll Center Parkway, Suite 160, Pleasanton, CA 94566, USA
Telephone: +1-925-3991568
E-mail: bpgoffice@wjgnet.com
Help Desk: https://www.f6publishing.com/helpdesk
https://www.wjgnet.com